iScience

CellPress

Article

High-Throughput Screening of Solid-State Li-Ion Conductors Using Lattice-Dynamics Descriptors

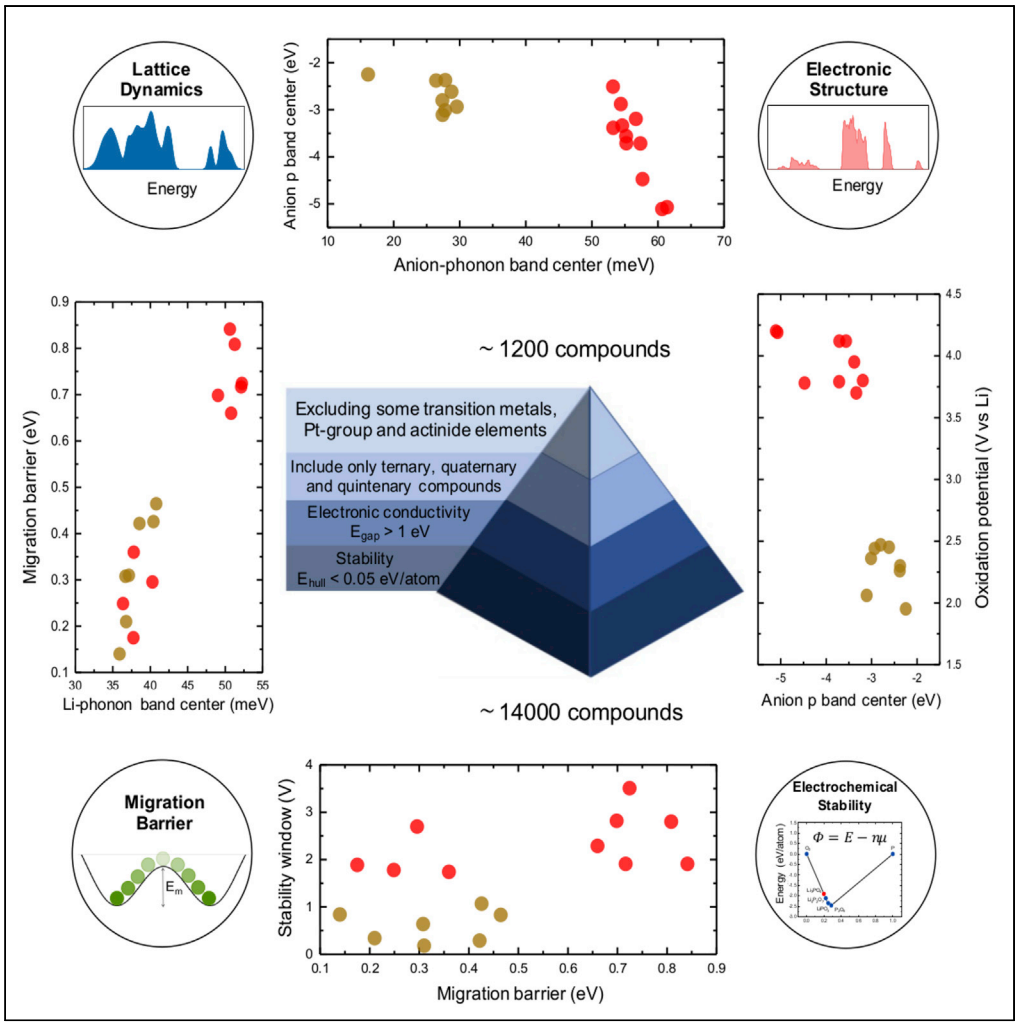

Sokseiha Muy, Johannes Voss, Roman Schlem, ..., Peter Lamp, Wolfgang G. Zeier, Yang Shao-Horn

sokseiha@mit.edu (S.M.)
vossj@slac.stanford.edu (J.V.)

HIGHLIGHTS

High-throughput screening of ~14,000 Li-containing compounds for new Li-ion conductors

A new method to compute phonon band center with only 2 DFT calculations per compound

One of the 18 predicted materials, Li_3ErCl_6 has ionic conductivity of 0.05–0.3 mS/cm

Muy et al., iScience *16*, 270–282
June 28, 2019
https://doi.org/10.1016/j.isci.2019.05.036

iScience

CellPress

Article

High-Throughput Screening of Solid-State Li-Ion Conductors Using Lattice-Dynamics Descriptors

Sokseiha Muy,[1,6,*] Johannes Voss,[2,*] Roman Schlem,[3] Raimund Koerver,[4] Stefan J. Sedlmaier,[4] Filippo Maglia,[4] Peter Lamp,[4] Wolfgang G. Zeier,[3] and Yang Shao-Horn[1,5]

SUMMARY

Low lithium-ion migration barriers have recently been associated with low average vibrational frequencies or phonon band centers, further helping identify descriptors for superionic conduction. To further explore this correlation, here we present the computational screening of ~14,000 Li-containing compounds in the Materials Project database using a descriptor based on lattice dynamics reported recently to identify new promising Li-ion conductors. An efficient computational approach was optimized to compute the average vibrational frequency or phonon band center of ~1,200 compounds obtained after pre-screening based on structural stability, band gap, and their composition. Combining a low computed Li phonon band center with large computed electrochemical stability window and structural stability, 18 compounds were predicted to be promising Li-ion conductors, one of which, Li_3ErCl_6, has been synthesized and exhibits a reasonably high room-temperature conductivity of 0.05–0.3 mS/cm, which shows the promise of Li-ion conductor discovery based on lattice dynamics.

INTRODUCTION

The use of organic liquid electrolytes (Xu, 2014) in the commercial Li-ion batteries (LIB) poses a major safety issue due to the high flammability of the solvent, which can lead to catastrophic fires (von Sacken et al., 1995). Replacing liquid electrolytes with inorganic solid-state lithium conductors will not only lower such safety concerns but also could potentially increase the energy density by reducing the volume of battery packing required to avoid leakage of liquid electrolytes and especially by hopefully enabling the use of lithium metal as the negative electrode (Janek and Zeier, 2016; Manthiram et al., 2017). Several structural and chemical families of solid Li-ion conductors such as LISICON (Kanno and Murayama, 2001; Khorassani and West, 1982; Rodger et al., 1985; Tachez et al., 1984) and Argyrodites (Deiseroth et al., 2011, 2008; Kong et al., 2010) have been shown to exhibit ionic conductivity spanning over 10 orders of magnitude at room temperature (RT) (Bachman et al., 2016). Since the discovery of lithium superionic conductor $Li_{10}GeP_2S_{12}$ (LGPS) by Kanno et al. (Kamaya et al., 2011) with RT ionic conductivity of 12 mS/cm, several compounds having RT Li-ion conductivity exceeding that of ethylene carbonate and dimethyl sulfite mixture (EC:DMS) with $LiPF_6$ (~10 mS/cm) have been discovered such as $Li_7P_3S_{11}$ (17 mS/cm) (Seino et al., 2014), argyrodite $Li_{6.6}Ge_{0.6}P_{0.4}S_5I$ (18 mS/cm) (Kraft et al., 2018), and LGPS-like $Li_{9.54}Si_{1.74}P_{1.44}S_{11.7}Cl_{0.3}$ (25 mS/cm) (Kato et al., 2016), which has the highest RT Li-ion conductivity to date. Unfortunately, these most conducting electrolytes have been shown to exhibit narrow electrochemical stability windows (~0.4 V for LGPS, 0.24 V for argyrodite Li_6PS_5Cl) (Richards et al., 2016; Zhu et al., 2015) and high chemical instability against electrode materials (Auvergniot et al., 2017; Han et al., 2016; Kato et al., 2016; Koerver et al., 2017b, 2017a; Xu et al., 2018). In addition, electrolytes have to be soft to accommodate volume expansion of the electrodes for several thousand cycles (Koerver et al., 2018) without cracking and prevent dendrite formation (Manthiram et al., 2017). These requirements impose very stringent conditions on the ideal candidate materials, which explains why to this date all-solid LIB using ceramic electrolytes are not yet on the market and the search for new materials and optimization of solid-state LIB is still an active area of research (Kerman et al., 2017; Takada, 2016; Zhang et al., 2018).

In recent years, the influence of the softness of a lattice, i.e., the average vibrational frequencies or phonon band center, has been shown to influence the ionic transport in solid electrolytes (Muy et al., 2018b, 2018a; Krauskopf et al., 2017, 2018b; Kraft et al., 2017). To further employ this understanding of the influence of lattice dynamics on ion mobility, in this article, we present the result

[1]Research Laboratory of Electronics, Massachusetts Institute of Technology, Cambridge, MA 02139, USA

[2]SUNCAT Center for Interface Science and Catalysis, SLAC National Accelerator Laboratory, 2575 Sand Hill Road, Menlo Park, CA 94025, USA

[3]Institute of Physical Chemistry & Center for Materials Research, Justus-Liebig-University Giessen, Heinrich-Buff-Ring 17, 35392 Giessen, Germany

[4]Research Battery Technology, BMW Group, 80788 Munich, Germany

[5]Department of Materials Science and Engineering, Massachusetts Institute of Technology, Cambridge, MA 02139, USA

[6]Lead Contact

*Correspondence: sokseiha@mit.edu (S.M.), vossj@slac.stanford.edu (J.V.)

https://doi.org/10.1016/j.isci.2019.05.036

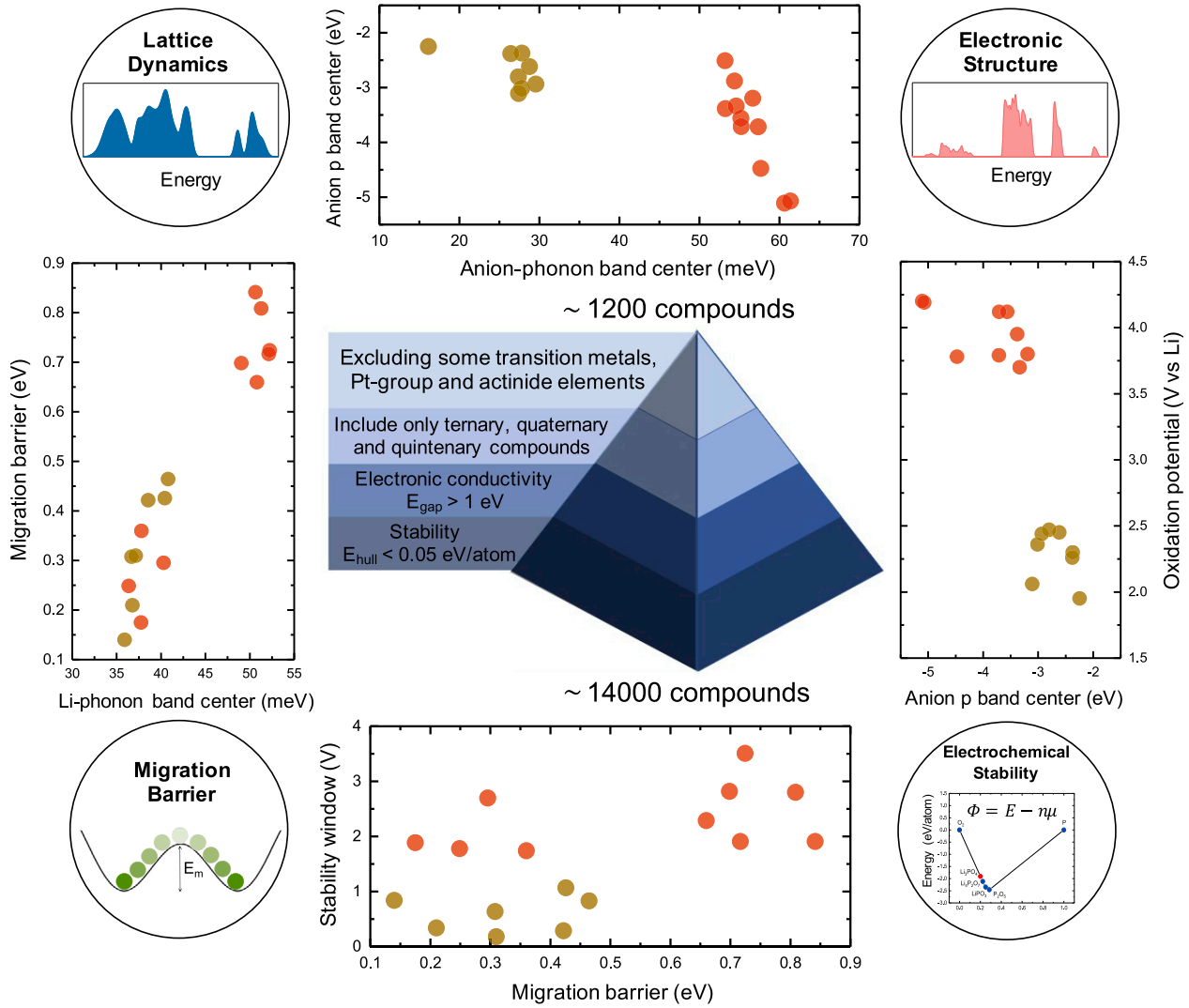

Figure 1. Schematic of the HT Screening as well as Various Correlations Studied in This Work

Electronic and phonon-related descriptors were shown to correlate with the migration barrier E_m and electrochemical stability of lithium-ion conductors. Data points in red correspond to oxides, whereas those in brown correspond to sulfides and were taken from previous work (Muy et al., 2018b).

of a high-throughput (HT) study of more than 1,000 Li-containing compounds using a lattice dynamic descriptor called the lithium-phonon band center, which is a measure of the average vibrational frequency of the lithium sublattice and has been proposed as a descriptor for the migration barrier or enthalpy of migration of lithium conductors in LISICON and olivine families (Muy et al., 2018b), in addition to several correlations between electronic structures, lattice dynamics, migration barrier, and electrochemical stability (Figure 1). Previous HT studies employed descriptors that were designed essentially based on static structural features (Avdeev et al., 2012; Wang et al., 2015) or using machine learning techniques to capture underlying correlations between the input features and the target properties from a database (Jalem et al., 2013; Sendek et al., 2018, 2017). For instance, Wang et al. (Wang et al., 2015) have proposed that a body-center cubic (BCC) structure provides the ideal framework for Li-ion conduction, where the deviation from the ideal BCC structure can be used as a descriptor for faster Li-ion conductors. Sendek et al. (Sendek et al., 2017) have used a logistic regression technique to train a model to classify a given material as superionic or normal Li-ion conductors. After training the model on a database of experimentally measured ionic conductivity, they used their model to classify several thousands of Li-containing compounds and suggested a few candidates that might exhibit superionic conductivity.

HT calculation of phonon-related properties has been hindered by the high computational cost associated with full density functional theory (DFT) calculations. Although HT infrastructure to compute vibrational properties of materials including phonon density of states (DOS) has been demonstrated enabling automatic workflow of phonon calculations to be executed with minimal human intervention (Petretto et al., 2018a), the computational time required for each phonon calculation is still high. To overcome the high computational cost associated with the calculation of phonon DOS using DFT (Petretto et al., 2018b), we employed and optimized an approximate method called *Quickhess*, which allowed us to compute phonon band center (at Γ-point) with only two single-point DFT calculations independent of the symmetry and size of the unit cell (Voss and Vegge, 2008). The computed phonon band centers with *Quickhess* exhibit accuracy comparable to the full DFT calculations. Moreover, we found a strong positive correlation between the computed total-phonon band centers and anion-phonon band centers, which are both related to the oxidation potential of Li-ion conductors. Lithium-phonon band centers exhibit only weak correlation with the total- and anion-phonon band centers. Based on the computed lithium-phonon band centers and the computed electrochemical windows, we proposed 18 compounds as promising Li-ion conductors, 17 of which ($LiCa_9Mg(PO_4)_7$, $Li_2Pr(NO_3)_5$, $LiPF_6$, $LiAsF_6$, $LiSbF_6$, LiK_2AlF_6, $Li_{10}Mg_7Cl_{24}$, Li_3ErCl_6, $LiCs_2LuCl_6$, $LiCs_2YCl_6$, Li_3CsCl_4, $LiYb_2Cl_5$, Li_2CsCl_3, $LiCsCl_2$, $LiRbBr_2$, Li_3ErBr_6, and $LiSr_4(BN_2)_3$) have not been reported to date. In addition to phonon band centers, we also examined the electronic band centers across different chemistries and found a negative correlation with the phonon band centers: the lower the phonon band centers, the closer the electronic anion p-band centers to the Fermi level. Finally, we also examined the correlation between the electrochemical stability and found a correlation between the oxidation potentials and the anion-phonon band centers, largely in agreement with previous study (Muy et al., 2018b). This work further strengthens the correlation of the phononic properties of the lattice to the stability and migration barriers by extending it to much larger chemical or structural families of Li-ion conductors, thus providing a new predictor of high ionic conductivity in HT screening approaches to find novel ionic conductors.

RESULTS AND DISCUSSIONS

Benchmark of Computed Phonon Band Centers Computed with *Quickhess*

To benchmark the accuracy of the *Quickhess* method, we have selected 53 compounds to cover several chemistries and structures of known Li-ion conductors and computed their phonon band centers within the full DFT calculations with finite-displacement method using the same parameters as in our previous work (Muy et al., 2018b). The computed phonon band centers of these 53 compounds using the *Quickhess* method was found to be comparable to those obtained from full DFT calculations once the parameter ε in Equation S2 was optimized. We tested two methods for choosing ε, one by referring it to the number of atoms in the unit cell and the other one by referring to the volume of the unit cell. We found that better accuracy was achieved by referring ε to the volume per ions in the unit cell, which is given by:

$$\varepsilon = \frac{\sqrt[3]{V_{cell}}}{N_1 . N_{atom}} \qquad \text{(Equation 1)}$$

where V_{cell} and N_{atom} are the volume of the unit cell and the number of atoms in the unit cell, respectively. The parameter N_1 was introduced to allow for variation of ε and for assessing its influence on the accuracy of the computed phonon band centers. The comparison of total-, anion-, and lithium-phonon band centers computed with full DFT (the computational details and different DFT parameters [number of K-points, plane-wave energy cutoff …] are the same as in our previous works; Muy et al., 2018b) and the *Quickhess* method using N_1=5 are shown in Figures 2A–2C, respectively. The agreement in the computed total and anion band centers from *Quickhess* with those obtained from full DFT is quite remarkable, with a mean absolute error (MAE) of only ~3.85 meV. However, the agreement in the computed lithium-phonon band center obtained from *Quickhess* is much worse, with MAE ~10.93 meV, which is too large for HT screening. Better accuracy of the lithium-phonon band center with *Quickhess* was obtained by employing one additional DFT calculation, where only the Li ions were displaced. This displacement was generated by adding all the Li-projected eigenvectors obtained in the previous step, and phonon energies were then again approximated using Equation S1 for h_i. A new DFT Hessian was constructed, and the new eigenvalues were extracted in exactly the same way as in the previous step. The length-scaling parameter

$$\varepsilon' = \frac{\sqrt[3]{V_{cell}}}{N_2 . N_{atom}} \qquad \text{(Equation 2)}$$

for this second displacement was again calibrated by extensive testing. The parameter N_2 allowed us to vary ε' and assess its influence on the accuracy of the computed phonon band centers. With this additional

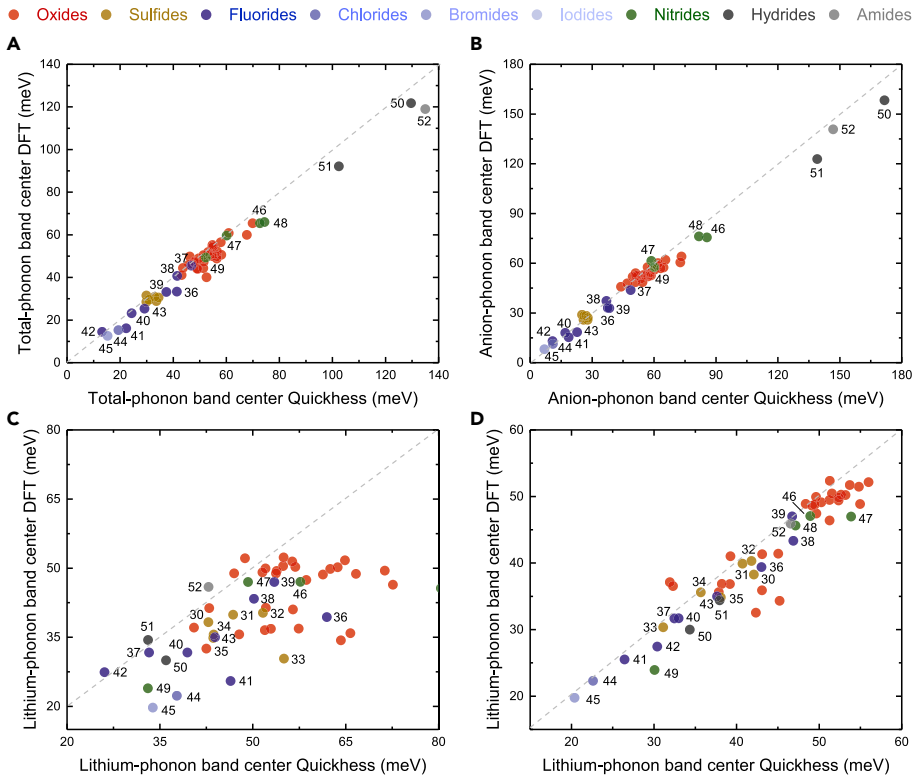

Figure 2. Comparison between Computed Band Centers Using Full DFT Calculations and *Quickhess* Method

(A–D) Comparison for (A) total-phonon band centers, (B) anion-phonon band centers, and (C) the Li-ion band centers. The agreement in the computed Li-ion phonon band centers between full DFT and *Quickhess* was improved significantly with one additional displacement constructed from the sum of Li-projected eigenvectors shown in (D). The oxides include Li_3XO_4 (X = P, As, Sb, V), Li_2XYO_4 (X = Na, Mg, Cd; Y=Si, As, Ge), $LiXYO_4$ (X = Mg, In, Sc, Al, Mn, Ni, Cd; Y = Si, Ge, As, P, V), $Li_{3.25}Ge_{0.25}X_{0.75}O_4$ (X = P, V), $Li_{3.25}Ge_{0.25}V_{0.75}O_4$, $Li_3V_{0.25}P_{0.75}O_4$, $LiAlO_2$, Li_6HfO_7, $LiNbO_3$, Li_2SnO_3, Li_8SnO_6, Li_4GeO_4, and sulfides Li_3SbS_4(31), Li_4XS_4 (X = Ge(35), Sn(36)), Li_2CdXS_4 (X = Si(32), Ge(33)); fluorides: Li_2ZrF_6(37), $LiPF_6$(38), Li_3AlF_6(39), $LiYF_4$(40); chlorides: Li_2MgCl_4(41), $LiSnCl_3$(42), $LiCsCl_2$(43), $LiAlCl_4$(44); bromides: Li_2ZnBr_4(45); Iodides: Li_2ZnI_4(46); nitrides: $LiPN_2$(47), Li_3BN_2(48), $LiSi_2N_3$(49), $LiSr_4(BN_2)_3$(50); hydrides: $LiBH_4$(51), $LiAlH_4$(52); and amides: $LiNH_2$(53). These computed phonon band centers from full DFT were taken from or computed with the same parameters as in previous work (Muy et al., 2018b).

step, the agreement between computed lithium-phonon band centers by *Quickhess* and full DFT was much improved, as shown in Figure 2D with N_2=10.

Computed lithium-phonon band centers with *Quickhess* were examined systematically by varying N_1 and N_2, where the MAE of lithium-phonon band centers smaller than 2.5 meV could be achieved with suitable values of N_1 and N_2, as shown in Figure S1. Based on these tests, N_1 = 2 and N_2 = 10 were chosen for all the computed phonon band centers shown in the remainder of this work. Moreover, in addition to the 53 compounds in Figure 2, we have also computed the lithium-phonon band centers of additional 72 compounds using the *Quickhess* method and compared them with the full DFT calculations available on Materials Project database (Figure S2). As these 72 compounds were not used during the optimization of the parameters N_1 and N_2, they can be viewed as our "validation set." The very good agreement between the *Quickhess* method and these 72 DFT calculations (Figure S2) further confirms the accuracy of our method. Finally, to test the robustness of our method, we computed the phonon band centers of all ~1,200 compounds using two sets of parameters N_1=2; N_2=10 and N_1=5; N_2=10. The difference in the computed phonon band centers by *Quickhess* with these two sets of N_1 and N_2 was found to fluctuate around zero as expected, with the exception of a few compounds, whose values of phonon band center change drastically upon variation of ε and ε' signaling potential issues (Figure S3). Based on this test, we excluded all compounds having difference in the computed phonon band centers with different sets of N_1 and N_2 larger than 5 meV resulting in ~1,000 compounds retained for the remaining part of the paper.

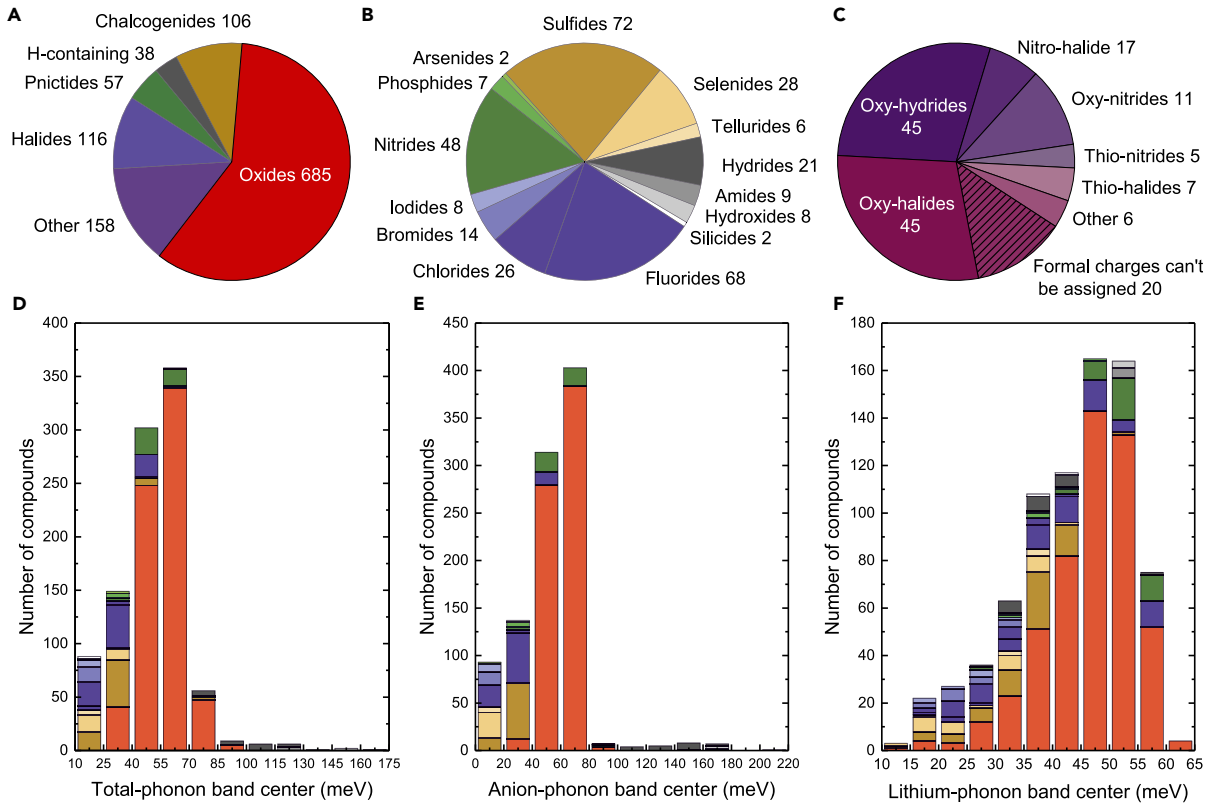

Figure 3. Number of Compounds and Phonon Band Center Distribution across Different Chemistries

(A–F) (A) The number of Li-containing compounds in each chemistry included in this study. (B) More detailed distribution of different families of compounds in each chemistry, excluding the oxides. (C) The distribution among the mixed-anion compounds and the number of compounds whose formal charge cannot be assigned using bond valence method. Histograms of (D) computed total-phonon band centers, (E) computed anion band centers, and (F) lithium-phonon band centers. Figures 3D–3F are replotted in Figure S4 excluding all oxides from the count to show the distribution of other chemistries more clearly.

Computed Phonon Band Centers of ~1,000 Li-Containing Inorganic Compounds by *Quickhess*

Total-, anion-, and lithium-phonon band centers of ~1,000 Li-containing inorganic compounds were computed by *Quickhess* (Figure 3). The most dominant chemistry in our study is the oxide family, which is followed by chalcogenides and halides and a smaller fraction of pnictides as well as hydrogen-containing compounds (essentially hydrides, hydroxides, and amides) (Figure 3A). A more detailed distribution of different chemistries is shown in Figure 3B, and the "other" compounds are shown in Figure 3C, which include mixed-anion compounds such as oxy-halides and oxy-nitrides. There are also a small number of compounds whose formal charge could not be assigned using the bond valence method, which are henceforth excluded from the analysis. The total-phonon band centers of oxides are centered at ~60 meV, whereas the total-phonon band centers of chalcogenides (sulfides, selenides and tellurides) were lower (Figure 3D), in agreement with previous work using 24 compounds (Muy et al., 2018b). In Figures S4A–S4C, the same histograms as Figure 3D excluding the oxide family are shown so that the distribution across other chemistries can be seen more clearly. Interestingly, the total-phonon band centers of fluorides are lower than for the oxides, on the order of 30 meV, whereas the total-phonon band centers of nitrides closely mirror those of the oxides. Hydrogen-containing compounds such as hydrides, hydroxides, and amides tend to have their total-phonon band centers skewed toward higher values owing to the small mass of the hydrogen atom (Figure 3D).

The histogram of anion-phonon band centers (Figure 3E) is similar to that of the total-phonon band centers, suggesting a strong correlation, which will be discussed in detail in the next section. In contrast, the histogram of lithium-phonon band centers (Figure 3F) is markedly different from those of total- and anion-phonon band centers, especially for the oxides. In agreement with our previous study (Muy et al.,

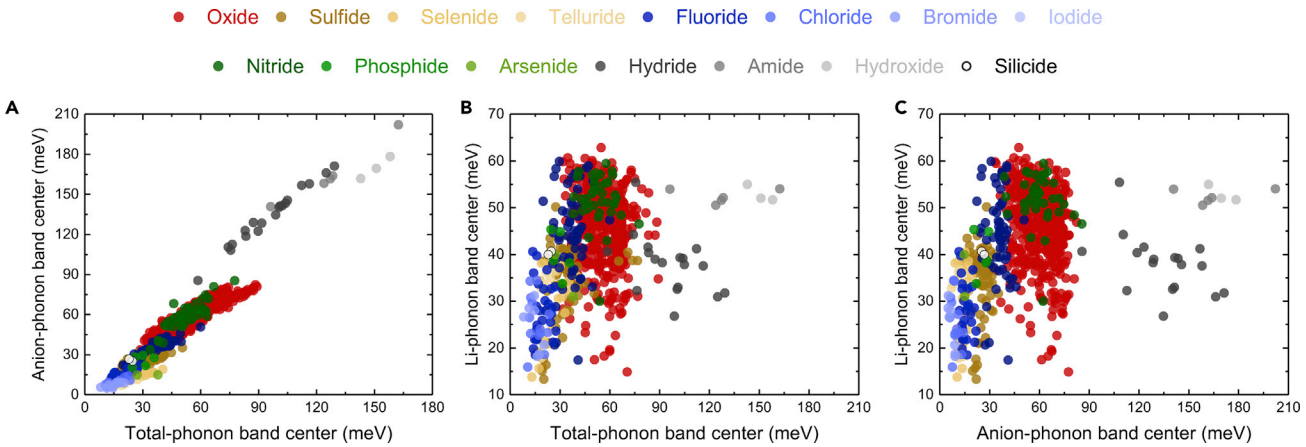

Figure 4. Correlations among Phonon Band Centers

(A–C) Correlation between (A) computed anion- and total-phonon band centers, (B) lithium-phonon band centers and total-phonon band centers, and (C) Li-phonon band centers and anion-phonon band centers of ~1,000 compounds shown in Figure 3 by *Quickhess*, excluding 158 with the mixed anions and those whose formal charge cannot be assigned.

2018b), most of the Li-phonon band centers of oxides tend to center at ~40–50 meV, whereas those of chalcogenides tend be lower, around 30–40 meV. It is of great interest to note that there are a significant number of oxides having particularly low Li-phonon band centers <30 meV, which are promising materials with potentially high mobility of Li-ions (Muy et al., 2018b) and will be discussed in more detail in a later section. Another noteworthy observation is that the Li-phonon band centers of some hydrides tend to be on the lower side of the distribution despite having very high total and anion band centers. This observation agrees with the experimental findings that several hydride lithium superionic conductors are known especially in their high-temperature phase (Matsuo et al., 2007; Mohtadi and Orimo, 2017).

It is significant to note that the computed anion-phonon band centers increase linearly with greater total-phonon band centers across a much larger structural and compositional space of ~1,000 Li-containing compounds, as shown in Figure 4A. In contrast, there is no correlation between Li- and total- (Figure 4B) or anion- (Figure 4C) phonon band centers within each chemical series (e.g., oxides, halides), although a broad linear correlation appears to exist across different chemistries. These results are in agreement with those of our previous study (Muy et al., 2018b) of 24 lithium-ion conductors in LISICON and olivine families, which show similar correlations between the total- and anion-phonon band centers, whereas the lithium-phonon band centers are essentially uncorrelated with other phonon band centers. Interestingly, there are a few oxides that have high total- and anion-phonon band centers (greater than ~40 meV) but relatively low Li-ion-phonon band centers (smaller than ~30 meV), indicating potentially low migration barriers. A common feature for compounds with low Li-ion-phonon band centers is the long Li-O bonds (1.9–2.5 Å) (Figure S5), where the average Li-anion bond distance appears to be the best descriptor for the Li-phonon band centers we found in this study. Some of these compounds are well-known Li-ion conductors (Enciso-Maldonado et al., 2015; Morgan et al., 2004; Muy et al., 2018b), including olivine $LiTmSiO_4$ (Jalem et al., 2012) or $LiInGeO_4$ (Jalem et al., 2012; Rajkumar et al., 2010) and NASICON-like compounds such as $LiM_2(PO_4)_3$ (M = Ge, Sn, and Zr) (Arbi et al., 2011; Martínez-Juárez et al., 1998; Winand et al., 1991). Less-well-known compounds include $LiLnO_2$ (Ln = Gd, Er and Lu), whose structures have been well characterized but have not been studied as Li-ion conductors (Cantwell et al., 2011; Hashimoto et al., 2002).

Correlation between Computed Phonon and Electronic Band Centers

Lowering the total- (Figure 5A) or anion- (Figure 5B) phonon band centers was found to scale with computed electronic anion p-band centers closer to the top of valence band. It is of great interest to relate anion-phonon band centers to electronic ligand band centers as anion p-band centers have been proposed as descriptors for catalytic activity (Lee et al., 2011), stability (Grimaud et al., 2013), and oxygen migration (Mayeshiba and Morgan, 2016) in perovskites. A strong correlation between the total- as well as anion-phonon band centers with the anion p-band centers (with respect to mid-gap) was found across different chemical series, whereas the correlation was much weaker within each chemical family, with the exception

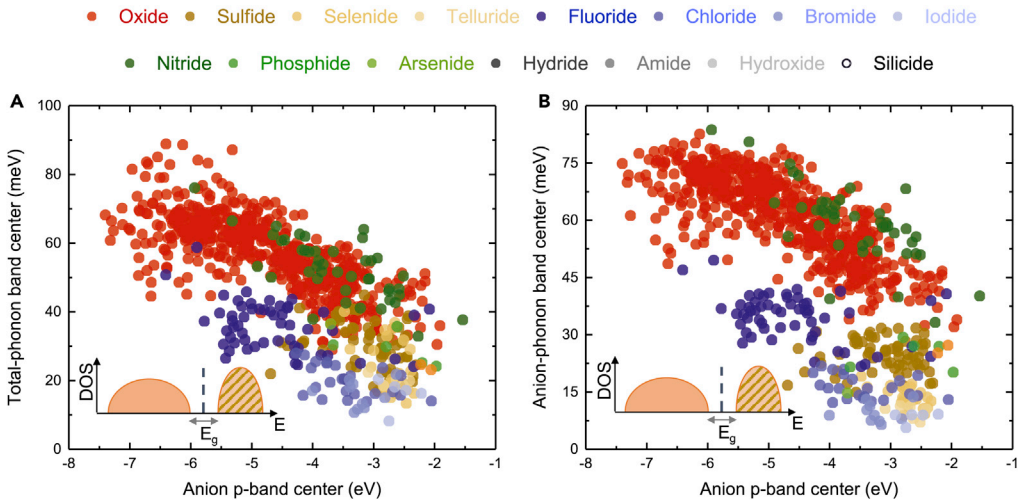

Figure 5. Correlations between Phonon Band Centers and Electronic p-band Centers

(A and B) Correlation between (A) computed total- and (B) anion-phonon band centers from *Quickhess* with computed anion electronic p-band centers of ~1,000 compounds. The inset shows the schematic of anion-projected electronic DOS. The anion p-band centers were computed by integrating over the occupied states with respect to the mid-gap indicated by the dashed line. Hydrogen-containing compounds (hydrides, hydroxides, and amides) were excluded due to the particular low mass of hydrogen and the difference in the nature of bonding, which involves the s-orbital instead of p-orbitals.

of oxides. Hydrogen-containing compounds (hydrides, hydroxides, and amides) were excluded owing to the low mass of hydrogen and the difference in the nature of bonding involving the s-orbital instead of p-orbitals. These trends remain valid if we used the top of the valence band instead of the mid gap as the reference for the anion p-band centers (Figure S6). As the electronic anion p-band center relative to the top of the valence band is a measure of covalency or ionicity (Hong et al., 2017), this correlation suggests that more covalent compounds tend to have lower vibrational frequencies of bonds involving nonmobile species. In contrast, no correlation was found between Li-phonon band centers and electronic band centers (Figure S7), which is in agreement with previous studies of 24 Li-ion conductors (Muy et al., 2018b).

Correlation between Electrochemical Stability and Phonon or Electron Band Centers

As the electrochemical stability of an electrolyte is governed by tendency of the material to give or accept electrons from the electrodes, which is in turn related to the positions of the conduction and valence band with respect to the Fermi level, the correlation between the anion p-band centers and anion-phonon band centers hints at the existence of another correlation between the electrochemical stability and phonon band centers. To quantify the electrochemical stability of these ~1,000 Li-containing compounds, we employed a computational method based on the construction of the grand-potential phase diagram (Richards et al., 2016; Zhu et al., 2016, 2015), which allowed us to compute the oxidation and reduction potential (versus Li^+/Li). In agreement with previous studies (Richards et al., 2016; Zhu et al., 2016, 2015), the oxidation potentials were largely determined by the nature of the anion in the structures, decreasing in the order from fluorides > chlorides ~ oxides > bromides > iodides ~ sulfides ~ selenides ~ tellurides > pnictides ~ hydrides, as shown in Figure 6A. In contrast, the reduction potentials show no apparent trend across any of the chemistries other than the fact that nitrides tend to be stable against reduction by lithium, in agreement with previous studies (Zhu et al., 2016, 2015). There are a few compounds that are both stable against reduction by lithium (having reduction potential ~0 V versus Li^+/Li) and against oxidation above 4 V versus Li^+/Li, highlighting the challenges to search for stable electrolytes in LIB. Moreover, the computed oxidation potentials were found to broadly increase with greater anion-phonon band (Figure 6B) and total-phonon band centers (Figure S8A), but not with lithium-phonon band centers (Figure S8B), in agreement with previous work of LISICON and olivine Li-ion conductors (Muy et al., 2018b). Specifically, the correlation falls into three separate groups, namely, group 15 (nitrides, phosphides, and arsenides), group 16 (oxides, sulfides, selenides, and tellurides), and group 17 (fluorides, chlorides, bromides, and iodides). This trend is consistent with the fact that compounds that have stiffer lattices and hence higher phonon energy (e.g., higher total- and anion-phonon band centers) are less covalent; having electronic anion p-band center

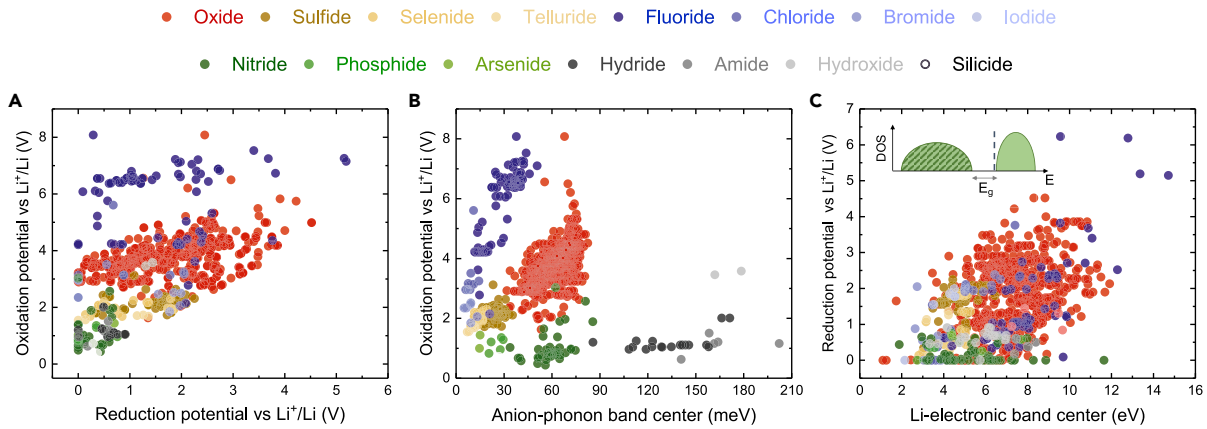

Figure 6. Computed Oxidation and Reduction Potentials and Their Correlations with Phonon and Electronic Band Centers

(A) Computed oxidation and reduction potential (versus Li^+/Li) for ~1,000 Li-containing compounds in the study.

(B) Correlation between computed oxidation potential and anion-phonon band center.

(C) Correlation between reduction potential and the electronic band center computed over the Li-projected conduction bands. The inset shows the schematic of the Li-projected electronic DOS. The Li-electronic band centers were computed by integrating over the unoccupied states with respect to the bottom of the conduction band indicated by the dashed line. All hydrogen-containing compounds (hydrides, hydroxides, and amides) fall into a separate region due to the very different nature of bonding in these compounds, which involves the s-orbital of hydrogen instead of p-orbitals of other anions and the particularly low mass of hydrogen.

further away from the top of valence band (Figure 5) correlates with greater oxidation potentials (more difficult to extract electrons from anion p-bands). This correlation is also consistent with the observation that the computed electrochemical stability windows, which are the difference between the computed oxidation and reduction potentials, increase with increasing band gap as expected (Figure S8F). Moreover, we found no correlation between the reduction potentials and the phonon band centers (Figures S8C–S8E) in agreement with previous study (Muy et al., 2018b). Interestingly, increasing reduction potentials were found to correlate with greater band centers of Li-projected electronic DOS integrated over the conduction band (Figure 4C). This trend could be rationalized by the following: the propensity of a material to be reduced is determined by the (thermodynamic) driving force to accept an electron to the conduction band, which can be approximately captured by the electronic band center computed over the conduction bands. Finally, we would like to emphasize that the correlations between phonon band centers, electronic band centers, and electrochemical stability are simply different manifestations of the covalency or ionicity across these materials, which are governed by the orbital overlap, electronegativity difference, and polarity between elements that make up the chemical bonds within these structures.

Prediction of Promising Li-Ion Conductors and Experimental Validation

By screening the phonon band centers and electrochemical stability of ~1,000 Li-containing compounds, 18 compounds were found to have small lithium-phonon band centers (less than 35 meV), key to have low lithium migration barrier, computed electrochemical stability window against oxidation and reduction larger than 3 V, and the energy above hull smaller than 20 meV/atom, which served as a proxy for structural stability, as shown in Figure 7. Only two oxides ($LiCa_9Mg(PO_4)_7$ and $Li_2Pr(NO_3)_5$) and no chalcogenide were found, which can be attributed to the fact that most of oxides having low Li phonon band center (Figure 4C) and chalcogenides tend to exhibit narrow electrochemical window (Figure 6A). Four fluorides (LiK_2AlF_6, $LiPF_6$, $LiAsF_6$, and $LiSbF_6$) possess large electrochemical window but relatively high lithium-band center, whereas the chloride family was noted prominently in Figure 7, having 10 chlorides that have high stability and low lithium-phonon band centers.

Although the poor electrochemical stability of known fast ionic conductors such as the thiophosphates is clearly problematic, one can still make use of their high ionic conductivity by exploiting their kinetic stability (Han et al., 2016; Park et al., 2018) and by using protective layers on electrode materials to extend their stability window. Therefore, we further relaxed the electrochemical stability criteria, and our screening study then includes several known Li-ion conductors such as the Li superionic conductor LGPS (Kamaya et al., 2011) and its derivative $Li_{10}SiP_2S_{12}$ (Kato et al., 2014) and $Li_{10}SnP_2S_{12}$ (Bron et al., 2013; Kato et al., 2014)

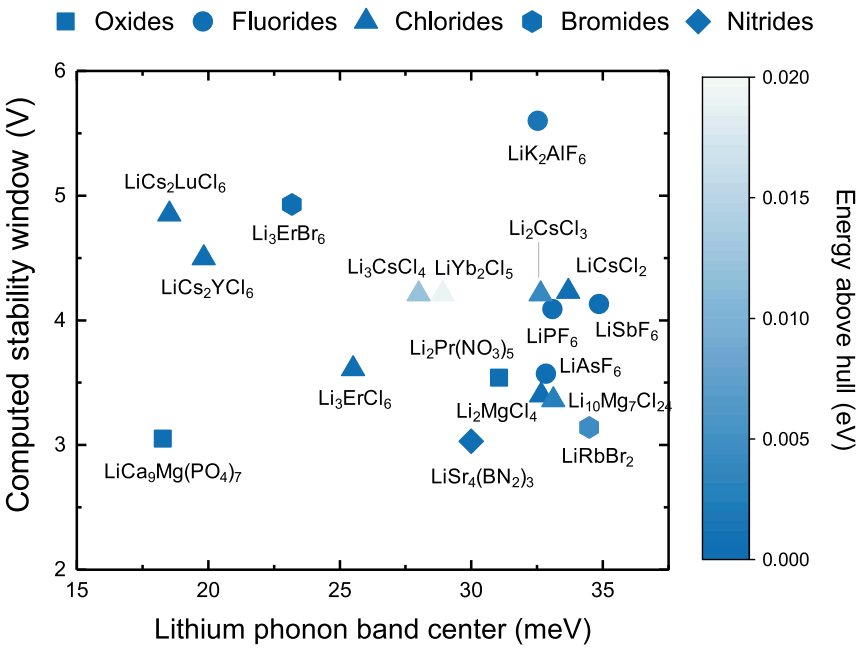

Figure 7. The 18 Most Promising Compounds Identified in This Study

These compounds were selected based on their stability window, which is larger than 3 V; Li-phonon band center smaller than 35 meV; along with their energy above hull, which serves as a proxy for their stability. Compounds having non-zero energy above hull are thermodynamically unstable at 0 K, although they can be stabilized at higher temperature by entropic contributions. Only two oxides and no chalcogenide are present due to their small stability windows, whereas only four fluorides are present despite having large electrochemical windows due to their high Li-phonon band centers. The most promising Li-ion conductors were found in the chloride family, which features prominently in the figure. A similar figure including compounds having stability window smaller than 3 V is shown in Figure S9, and numerical values of all compounds along with their unique MP identifiers are shown in Table S1.

as can be seen in Figure S9. In addition, we recovered lithium borohydride $LiBH_4$, which was one of the first Li superionic conductor discovered in the hydride family (Matsuo et al., 2007). Similarly, our results indicated that the lower stability electrolytes such as Li_3InCl_6 and Li_6MgBr_8 are good Li-ion conductors in agreement with the experimental finding that the ionic conductivity of the solid solution $Li_3InBr_{6-x}Cl_x$ is on the order of 0.05–2 mS/cm (Tomita et al., 2008; Yamada et al., 2006). Our results also include previously predicted fast Li-ion conductors using a machine learning technique (logistic regression) such as $Li_5B_7S_{13}$, Li_3ErCl_6, LiKTe, … (Sendek et al., 2018, 2017) (Figure S9). Numerical values of stability window, lithium-phonon band center, and energy above hull of all compounds shown in Figures 7 and S9 along with their unique Materials Project ID are given in Table S1.

More recently, two Li-ion conductors Li_3YCl_6 and Li_3YBr_6, which are structurally and chemically very similar to Li_3ErCl_6 and Li_3ErBr_6 in Figure 7, have been shown to have high ionic conductivity ~1 mS/cm and good cycling performance in all-solid-state batteries (Asano et al., 2018). Based on this study and to further validate the results of our HT screening, we have synthesized one of the predicted materials, Li_3ErCl_6. The structure of Li_3ErCl_6 was initially solved by Bohnsack et al. using single crystals obtained by a slow-cooling synthesis method of a stoichiometric mixture of $ErCl_3$ and LiCl, and the structure is shown in Figure 8A (Bohnsack et al., 1997). The chloride atoms build up a hexagonally closed packed lattice with octahedral voids that are partially occupied. Every $ErCl_6^{3-}$ octahedron is surrounded by six $LiCl_6^{6-}$ octahedra. X-ray diffraction was used to characterize the samples and further investigate the structure. Figure 8B shows the diffraction patterns for the ball-milled sample directly after the synthesis and after subsequent annealing. The diffraction pattern collected directly after the ball-milling process exhibits broad reflections with low intensity, owing to the strong amorphization during the ball milling. The diffraction pattern for the crystalline sample that was collected after subsequent annealing of the ball-milled sample can be indexed to the trigonal space group $P\bar{3}m1$. A Pawley fit leads to the lattice parameters $a = b = 11.1693(2)$ and $c = 6.0363(1)$. A minor amount of around 5 $\pm$ 1 wt. % LiCl impurity was found to exist using a tentative Rietveld

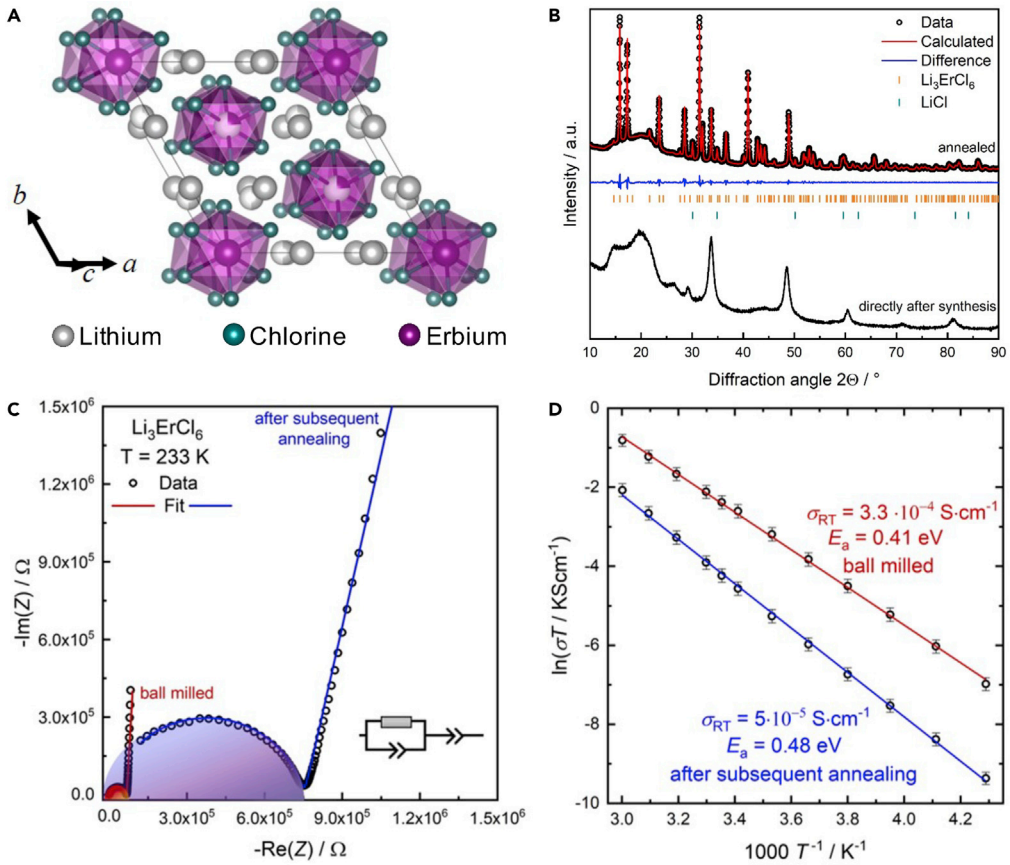

Figure 8. Synthesis, Structural Characterization, and EIS Measurements of Li_3ErCl_6

(A) Structural features within the unit cell, showing face-sharing $ErCl_6^{3-}$ octahedra with Li^+ in chains along the *c*-axis.

(B) Comparison of the diffraction patterns for the synthesized Li_3ErCl_6 compounds directly after milling (bottom) and subsequent crystallization (top).

(C and D) (C) Comparison of exemplary impedance data at −30°C and (D) Arrhenius plot showing the room-temperature conductivities and activation barriers for ionic motion.

refinement. However, due to the low scattering form factor of Li no full structural characterization by a Rietveld refinement was performed.

AC impedance spectroscopy was performed to assess the ionic conductivity and activation barriers for ion migration within the synthesized materials. The Nyquist plots of the impedance data collected at 233 K can be found in Figure 8C, and the corresponding Arrhenius plots can be found in Figure 8D. The impedance data for every measured temperature were fit using one parallel constant phase element (CPE)—resistor unit, which is fit in series to another CPE that represents the gold electrodes. The capacitances C of the combination R/CPE where estimated using the Brug formula (Brug et al., 1984). Although no contribution of bulk and grain boundaries can be seen, the obtained capacitances (48 pF/cm^2) and ideality factor α of >0.85 correspond well with bulk transport. The obtained conductivities and activation barriers for Li_3ErCl_6 are 0.3 mS/cm (E_A = 0.41 eV) and 0.05 mS/cm (E_A = 0.48 eV) for the ball-milled and the crystalline samples, respectively. The ball-milled sample without subsequent annealing has a noticeably increased conductivity. It has been previously shown that ball-milled samples exhibit a higher conductivity, likely related to introducing defects while using the harsh conditions of ball milling, or resulting from subtle structural changes in the glassy state (Krauskopf et al., 2018a).

Further structural studies will be needed to elucidate the underlying reasons for the difference in the ionic conductivity between the samples in depth; however, these results clearly show that the HT screening of materials proposed for novel ionic conductors is successful. We expect that the ionic conductivity can

be further enhanced with the compositional optimization, for example, via aliovalent substitution to optimize the concentration of mobile species (Culver et al., 2018). Besides Li_3ErCl_6, as synthesized in this work, and Li_2MgCl_4 (Lutz et al., 1981; Nagel et al., 2002), to the best of the authors' knowledge no other compound in Figure 7 has been studied as Li-ion conductor with the exception of $LiPF_6$, $LiAsF_6$, and $LiSbF_6$, which are used as lithium salts in liquid electrolytes (Xu, 2014), therefore representing an exciting opportunity to discover new families of Li-ion conductors having potentially both high ionic conductivity and electrochemical stability.

Limitations of the Study

We would like to emphasize that the lithium-phonon band center has been proposed as a descriptor for the *migration barrier* which, in stoichiometric compounds, is not the same as the measured activation energy, which also contains contribution from defect formation energy. To exhibit high ionic conductivity, optimal concentration of mobile species is also needed in addition to low migration barrier. Therefore, aliovalent substitution might be necessary, and thus a complementary computational study of dopability might also be necessary. Finally, the migration barriers we considered here are only indicative of the local jumps between two adjacent sites. These sites have to be connected to form a percolating network for the long-range diffusion to occur. Therefore, additional study for the presence of percolating pathways in the structures is necessary to fully assess the potential of these materials as new lithium superionic conductors.

METHODS

All methods can be found in the accompanying Transparent Methods supplemental file.

SUPPLEMENTAL INFORMATION

Supplemental Information can be found online at https://doi.org/10.1016/j.isci.2019.05.036.

ACKNOWLEDGMENTS

This research used resources of the National Energy Research Scientific Computing Center, a DOE Office of Science User Facility supported by the Office of Science of the U.S. Department of Energy under Contract No. DE-AC02-05CH11231. J.V. acknowledges support by the US Department of Energy, Chemical Sciences, Geosciences, and Biosciences (CSGB) Division of the Office of Basic Energy Sciences, via Grant DE-AC02-76SF00515 to the SUNCAT Center for Interface Science and Catalysis. R.S. and W.G.Z. gratefully acknowledge the support by the Deutsche Forschungsgemeinschaft (DFG) under grant number ZE 1010/4-1.

AUTHOR CONTRIBUTIONS

S.M., Y.S.-H., and J.V. proposed the general concept of the paper. S.M. and J.V. modified and optimized the *Quickhess* code for HT screening. S.M. performed the HT computations and screenings. R.S. and W.G.Z. synthesized Li_3ErCl_6 and performed all the XRD and EIS measurements. S.M.Y. S.-H., J.V., R.S., and W.G.Z. wrote the manuscript. All authors contributed to the discussion and revision of the manuscript. All authors have given approval to the final version of the manuscript.

DECLARATION OF INTERESTS

The authors declare no competing interests.

Received: March 5, 2019
Revised: April 11, 2019
Accepted: May 23, 2019
Published: June 28, 2019

REFERENCES

Arbi, K., París, M.A., and Sanz, J. (2011). Li mobility in Nasicon-type materials $LiM_2(PO_4)_3$, M = Ge, Ti, Sn, Zr and Hf, followed by ^{7}Li NMR spectroscopy. Dalton Trans. *40*, 10195–10202.

Asano, T., Sakai, A., Ouchi, S., Sakaida, M., Miyazaki, A., and Hasegawa, S. (2018). Solid halide electrolytes with high lithium-ion conductivity for application in 4 V class bulk-type all-solid-state batteries. Adv. Mater. *30*, e1803075.

Auvergniot, J., Cassel, A., Ledeuil, J.-B., Viallet, V., Seznec, V., and Dedryvère, R. (2017). Interface stability of argyrodite Li_6PS_5Cl toward $LiCoO_2$, $LiNi_{1/3}Co_{1/3}Mn_{1/3}O_2$, and $LiMn_2O_4$ in bulk all-solid-state batteries. Chem. Mater. *29*, 3883–3890.

Avdeev, M., Sale, M., Adams, S., and Rao, R.P. (2012). Screening of the alkali-metal ion

containing materials from the Inorganic Crystal Structure Database (ICSD) for high ionic conductivity pathways using the bond valence method. Solid State Ion. *225*, 43–46.

Bachman, J.C., Muy, S., Grimaud, A., Chang, H.-H., Pour, N., Lux, S.F., Paschos, O., Maglia, F., Lupart, S., Lamp, P., et al. (2016). Inorganic solid-state electrolytes for lithium batteries: mechanisms and properties governing ion conduction. Chem. Rev. *116*, 140–162.

Bohnsack, A., Stenzel, F., Zajonc, A., Balzer, G., Wickleder, M.S., and Meyer, G. (1997). Ternäre Halogenide vom Typ A_3MX_6. VI [1]. Ternäre Chloride der Selten-Erd-Elemente mit Lithium, Li_3MCl_6 (M = Tb-Lu, Y, Sc): synthese, kristallstrukturen und ionenbewegung. Z. Anorg. Allg. Chem. *623*, 1067–1073.

Bron, P., Johansson, S., Zick, K., Schmedt auf der Günne, J., Dehnen, S., and Roling, B. (2013). $Li_{10}SnP_2S_{12}$: an affordable lithium superionic conductor. J. Am. Chem. Soc. *135*, 15694–15697.

Brug, G.J., van den Eeden, A.L.G., Sluyters-Rehbach, M., and Sluyters, J.H. (1984). The analysis of electrode impedances complicated by the presence of a constant phase element. J. Electroanal. Chem. Interfacial Electrochem. *176*, 275–295.

Cantwell, J.R., Roof, I.P., Smith, M.D., and zur Loye, H.-C. (2011). Crystal growth and optical properties of lithium–lanthanide oxides: $LiLnO_2$ (Ln = Nd, Sm, Eu, Gd and Dy). Solid State Sci. *13*, 1006–1012.

Culver, S.P., Koerver, R., Krauskopf, T., and Zeier, W.G. (2018). Designing ionic conductors: the interplay between structural phenomena and interfaces in thiophosphate-based solid-state batteries. Chem. Mater. *30*, 4179–4192.

Deiseroth, H.-J., Kong, S.-T., Eckert, H., Vannahme, J., Reiner, C., Zaiß, T., and Schlosser, M. (2008). Li_6PS_5X: a class of crystalline Li-rich solids with an unusually high Li^+ mobility. Angew. Chem. Int. Ed. *47*, 755–758.

Deiseroth, H.-J., Maier, J., Weichert, K., Nickel, V., Kong, S.-T., and Reiner, C. (2011). Li_7PS_6 and Li_6PS_5X (X: Cl, Br, I): possible three-dimensional diffusion pathways for lithium ions and temperature dependence of the ionic conductivity by impedance measurements. Z. Anorg. Allg. Chem. *637*, 1287–1294.

Enciso-Maldonado, L., Dyer, M.S., Jones, M.D., Li, M., Payne, J.L., Pitcher, M.J., Omir, M.K., Claridge, J.B., Blanc, F., and Rosseinsky, M.J. (2015). Computational identification and experimental realization of lithium vacancy introduction into the olivine $LiMgPO_4$. Chem. Mater. *27*, 2074–2091.

Grimaud, A., May, K.J., Carlton, C.E., Lee, Y.-L., Risch, M., Hong, W.T., Zhou, J., and Shao-Horn, Y. (2013). Double perovskites as a family of highly active catalysts for oxygen evolution in alkaline solution. Nat. Commun. *4*, 2439.

Han, F., Zhu, Y., He, X., Mo, Y., and Wang, C. (2016). Electrochemical stability of $Li_{10}GeP_2S_{12}$ and $Li_7La_3Zr_2O_{12}$ solid electrolytes. Adv. Energy Mater. *6*, 1501590–1501598.

Hashimoto, Y., Wakeshima, M., Matsuhira, K., Hinatsu, Y., and Ishii, Y. (2002). Structures and magnetic properties of ternary lithium oxides $LiRO_2$ (R = Rare Earths). Chem. Mater. *14*, 3245–3251.

Hong, W.T., Stoerzinger, K.A., Lee, Y.-L., Giordano, L., Grimaud, A., Johnson, A.M., Hwang, J., Crumlin, E.J., Yang, W., and Shao-Horn, Y. (2017). Charge-transfer-energy-dependent oxygen evolution reaction mechanisms for perovskite oxides. Energy Environ. Sci. *10*, 2190–2200.

Jalem, R., Aoyama, T., Nakayama, M., and Nogami, M. (2012). Multivariate method-assisted Ab Initio study of olivine-type $LiMXO_4$ (Main Group M^{2+}–X^{5+} and M^{3+}–X^{4+}) compositions as potential solid electrolytes. Chem. Mater. *24*, 1357–1364.

Jalem, R., Nakayama, M., and Kasuga, T. (2013). An efficient rule-based screening approach for discovering fast lithium ion conductors using density functional theory and artificial neural networks. J. Mater. Chem. A *2*, 720–734.

Janek, J., and Zeier, W.G. (2016). A solid future for battery development. Nat. Energy *1*, 16141.

Kamaya, N., Homma, K., Yamakawa, Y., Hirayama, M., Kanno, R., Yonemura, M., Kamiyama, T., Kato, Y., Hama, S., Kawamoto, K., and Mitsui, A. (2011). A lithium superionic conductor. Nat. Mater. *10*, 682–686.

Kanno, R., and Murayama, M. (2001). Lithium ionic conductor Thio-LISICON: the Li_2S - GeS_2 - P_2S_5 system. J. Electrochem. Soc. *148*, A742–A746.

Kato, Y., Hori, S., Saito, T., Suzuki, K., Hirayama, M., Mitsui, A., Yonemura, M., Iba, H., and Kanno, R. (2016). High-power all-solid-state batteries using sulfide superionic conductors. Nat. Energy. https://doi.org/10.1038/nenergy.2016.30.

Kato, Y., Saito, R., Sakano, M., Mitsui, A., Hirayama, M., and Kanno, R. (2014). Synthesis, structure and lithium ionic conductivity of solid solutions of $Li_{10}(Ge_{1-x}M_x)P_2S_{12}$ (M = Si, Sn). J. Power Sources *271*, 60–64.

Kerman, K., Luntz, A., Viswanathan, V., Chiang, Y.-M., and Chen, Z. (2017). Review—practical challenges hindering the development of solid state Li ion batteries. J. Electrochem. Soc. *164*, A1731–A1744.

Khorassani, A., and West, A. (1982). New Li^+ ion conductors in the system Li_4SiO_4-Li_3AsO_4. Solid State Ion. *7*, 1–8.

Koerver, R., Aygün, I., Leichtweiß, T., Dietrich, C., Zhang, W., Binder, J.O., Hartmann, P., Zeier, W.G., and Janek, J. (2017a). Capacity fade in solid-state batteries: interphase formation and chemomechanical processes in Nickel-rich layered oxide cathodes and lithium thiophosphate solid electrolytes. Chem. Mater. *29*, 5574–5582.

Koerver, R., Walther, F., Aygün, I., Sann, J., Dietrich, C., Zeier, W.G., and Janek, J. (2017b). Redox-active cathode interphases in solid-state batteries. J. Mater. Chem. A *5*, 22750–22760.

Koerver, R., Zhang, W., Biasi, L., de Schweidler, S., Kondrakov, A.O., Kolling, S., Brezesinski, T., Hartmann, P., Zeier, W.G., and Janek, J. (2018). Chemo-mechanical expansion of lithium electrode materials – on the route to mechanically optimized all-solid-state batteries. Energy Environ. Sci. *11*, 2142–2158.

Kong, S.-T., Deiseroth, H.-J., Maier, J., Nickel, V., Weichert, K., and Reiner, C. (2010). Li_6PO_5Br and Li_6PO_5Cl: the first lithium-oxide-argyrodites. Z. Anorg. Allg. Chem. *636*, 1920–1924.

Kraft, M.A., Culver, S.P., Calderon, M., Böcher, F., Krauskopf, T., Senyshyn, A., Dietrich, C., Zevalkink, A., Janek, J., and Zeier, W.G. (2017). Influence of lattice polarizability on the ionic conductivity in the lithium superionic argyrodites Li_6PS_5X (X = Cl, Br, I). J. Am. Chem. Soc. *139*, 10909–10918.

Kraft, M.A., Ohno, S., Zinkevich, T., Koerver, R., Culver, S.P., Fuchs, T., Senyshyn, A., Indris, S., Morgan, B.J., and Zeier, W.G. (2018). Inducing high ionic conductivity in the lithium superionic argyrodites $Li_{6+x}P_{1-x}Ge_xS_5I$ for all-solid-state batteries. J. Am. Chem. Soc. *140*, 16330–16339.

Krauskopf, T., Culver, S.P., and Zeier, W.G. (2018a). Local tetragonal structure of the cubic superionic conductor Na_3PS_4. Inorg. Chem. *57*, 4739–4744.

Krauskopf, T., Muy, S., Culver, S.P., Ohno, S., Delaire, O., Shao-Horn, Y., and Zeier, W.G. (2018b). Comparing the descriptors for investigating the influence of lattice dynamics on ionic transport using the superionic conductor $Na_3PS_{4-x}Se_x$. J. Am. Chem. Soc. *140*, 14464–14473.

Krauskopf, T., Pompe, C., Kraft, M.A., and Zeier, W.G. (2017). Influence of lattice dynamics on Na+ transport in the solid electrolyte $Na_3PS_{4-x}Se_x$. Chem. Mater. *29*, 8859–8869.

Lee, Y.-L., Kleis, J., Rossmeisl, J., Shao-Horn, Y., and Morgan, D. (2011). Prediction of solid oxide fuel cell cathode activity with first-principles descriptors. Energy Environ. Sci. *4*, 3966–3970.

Lutz, H.D., Schmidt, W., and Haeuseler, H. (1981). Chloride spinels: a new group of solid lithium electrolytes. J. Phys. Chem. Solids *42*, 287–289.

Manthiram, A., Yu, X., and Wang, S. (2017). Lithium battery chemistries enabled by solid-state electrolytes. Nat. Rev. Mater. *2*. https://doi.org/10.1038/natrevmats.2016.103.

Martínez-Juárez, A., Pecharromán, C., Iglesias, J.E., and Rojo, J.M. (1998). Relationship between activation energy and bottleneck size for Li^+ ion conduction in NASICON materials of composition $LiMM'(PO_4)_3$; M, M' = Ge, Ti, Sn, Hf. J. Phys. Chem. B *102*, 372–375.

Matsuo, M., Nakamori, Y., Orimo, S., Maekawa, H., and Takamura, H. (2007). Lithium superionic conduction in lithium borohydride accompanied by structural transition. Appl. Phys. Lett. *91*, 224103.

Mayeshiba, T.T., and Morgan, D.D. (2016). Factors controlling oxygen migration barriers in perovskites. Solid State Ion. *296*, 71–77.

Mohtadi, R., and Orimo, S. (2017). The renaissance of hydrides as energy materials. Nat. Rev. Mater. *2*. https://doi.org/10.1038/natrevmats.2016.91.

Morgan, D., Ven, A.V., and der Ceder, G. (2004). Li conductivity in Li_xMPO_4 (M = Mn, Fe, Co, Ni)

olivine materials. Electrochem. Solid State Lett. *7*, A30–A32.

Muy, S., Bachman, J.C., Chang, H.-H., Giordano, L., Maglia, F., Lupart, S., Lamp, P., Zeier, W.G., and Shao-Horn, Y. (2018a). Lithium conductivity and Meyer-Neldel rule in Li_3PO_4–Li_3VO_4–Li_4GeO_4 lithium superionic conductors. Chem. Mater. *30*, 5573–5582.

Muy, S., Bachman, J.C., Giordano, L., Chang, H.-H., Abernathy, D.L., Bansal, D., Delaire, O., Hori, S., Kanno, R., Maglia, F., et al. (2018b). Tuning mobility and stability of lithium ion conductors based on lattice dynamics. Energy Environ. Sci. *11*, 850–859.

Nagel, R., Groß, Th.W., Günther, H., and Lutz, H.D. (2002). ^{6}Li and ^{7}Li MAS nmr studies on fast ionic conducting spinel-Type Li_2MgCl_4, $Li_{2-x}Cu_xMgCl_4$, $Li_{2-x}Na_xMgCl_4$, and Li_2ZnCl_4. J. Solid State Chem. *165*, 303–311.

Park, K.H., Bai, Q., Kim, D.H., Oh, D.Y., Zhu, Y., Mo, Y., and Jung, Y.S. (2018). Design strategies, practical considerations, and new solution processes of sulfide solid electrolytes for all-solid-state batteries. Adv. Energy Mater. *8*, 1800035.

Petretto, G., Dwaraknath, S., Miranda, H.P.C., Winston, D., Giantomassi, M., van Setten, M.J., Gonze, X., Persson, K.A., Hautier, G., and Rignanese, G.-M. (2018a). High-throughput density-functional perturbation theory phonons for inorganic materials. Sci. Data *5*, 180065.

Petretto, G., Gonze, X., Hautier, G., and Rignanese, G.-M. (2018b). Convergence and pitfalls of density functional perturbation theory phonons calculations from a high-throughput perspective. Comput. Mater. Sci. *144*, 331–337.

Rajkumar, T., Nakayama, M., and Nogami, M. (2010). Ab initio prediction for the ionic conduction of lithium in and olivine materials. Solid State Commun. *150*, 693–696.

Richards, W.D., Miara, L.J., Wang, Y., Kim, J.C., and Ceder, G. (2016). Interface stability in solid-state batteries. Chem. Mater. *28*, 266–273.

Rodger, A., Kuwano, J., and West, A. (1985). Li+ ion conducting gamma-solid solutions in the systems Li_4XO_4-Li_3YO_4 - X=Si,Ge,Ti; Y=P,As,V; Li_4XO_4-$LiZO_2$-Z=Al,Ga,Cr and Li_4GeO_4-Li_2CaGeO_4. Solid State Ion. *15*, 185–198.

Seino, Y., Ota, T., Takada, K., Hayashi, A., and Tatsumisago, M. (2014). A sulphide lithium super ion conductor is superior to liquid ion conductors for use in rechargeable batteries. Energy Environ. Sci. *7*, 627–631.

Sendek, A.D., Cubuk, E.D., Antoniuk, E.R., Cheon, G., Cui, Y., and Reed, E.J. (2018). Machine learning-assisted discovery of solid Li-Ion conducting materials. Chem. Mater.. https://doi.org/10.1021/acs.chemmater.8b03272

Sendek, A.D., Yang, Q., Cubuk, E.D., Duerloo, K.-A.N., Cui, Y., and Reed, E.J. (2017). Holistic computational structure screening of more than 12000 candidates for solid lithium-ion conductor materials. Energy Environ. Sci. *10*, 306–320.

Tachez, M., Malugani, J.-P., Mercier, R., and Robert, G. (1984). Ionic conductivity of and phase transition in lithium thiophosphate Li_3PS_4. Solid State Ion. *14*, 181–185.

Takada, K. (2016). Solid electrolytes and solid-state batteries. AIP Conf. Proc. *1765*, 020008.

Tomita, Y., Matsushita, H., Kobayashi, K., Maeda, Y., and Yamada, K. (2008). Substitution effect of ionic conductivity in lithium ion conductor, $Li_3InBr_{6-x}Cl_x$. Solid State Ion. *179*, 867–870.

von Sacken, U., Nodwell, E., Sundher, A., and Dahn, J.R. (1995). Comparative thermal stability of carbon intercalation anodes and lithium metal anodes for rechargeable lithium batteries. J. Power Sources *54*, 240–245.

Voss, J., and Vegge, T. (2008). Γ-point lattice free energy estimates from O(1) force calculations. J. Chem. Phys. *128*, 184708.

Wang, Y., Richards, W.D., Ong, S.P., Miara, L.J., Kim, J.C., Mo, Y., and Ceder, G. (2015). Design principles for solid-state lithium superionic conductors. Nat. Mater. *14*, 1026–1031.

Winand, J.-M., Rulmont, A., and Tarte, P. (1991). Nouvelles solutions solides $Li(M^{IV})_{2-x}(N^{IV})_x(PO_4)_3$ (L = Li,Na M, N = Ge,Sn,Ti,Zr,Hf) synthèse et étude par diffraction x et conductivité ionique. J. Solid State Chem. *93*, 341–349.

Xu, K. (2014). Electrolytes and interphases in Li-ion batteries and beyond. Chem. Rev. *114*, 11503–11618.

Xu, L., Tang, S., Cheng, Y., Wang, K., Liang, J., Liu, C., Cao, Y.-C., Wei, F., and Mai, L. (2018). Interfaces in solid-state lithium batteries. Joule *2*, 1991–2015.

Yamada, K., Kumano, K., and Okuda, T. (2006). Lithium superionic conductors Li_3InBr_6 and $LiInBr_4$ studied by ^{7}Li, ^{115}In NMR. Solid State Ion. *177*, 1691–1695.

Zhang, Z., Shao, Y., Lotsch, B., Hu, Y.-S., Li, H., Janek, J., Nazar, L.F., Nan, C.-W., Maier, J., Armand, M., and Chen, L. (2018). New horizons for inorganic solid state ion conductors. Energy Environ. Sci. *11*, 1945–1976.

Zhu, Y., He, X., and Mo, Y. (2016). First principles study on electrochemical and chemical stability of solid electrolyte–electrode interfaces in all-solid-state Li-ion batteries. J. Mater. Chem. A *4*, 3253–3266.

Zhu, Y., He, X., and Mo, Y. (2015). Origin of outstanding stability in the lithium solid electrolyte materials: insights from thermodynamic analyses based on first-principles calculations. ACS Appl. Mater. Interfaces *7*, 23685–23693.

ISCI, Volume *16*

Supplemental Information

High-Throughput Screening of Solid-State Li-Ion Conductors Using Lattice-Dynamics Descriptors

Sokseiha Muy, Johannes Voss, Roman Schlem, Raimund Koerver, Stefan J. Sedlmaier, Filippo Maglia, Peter Lamp, Wolfgang G. Zeier, and Yang Shao-Horn

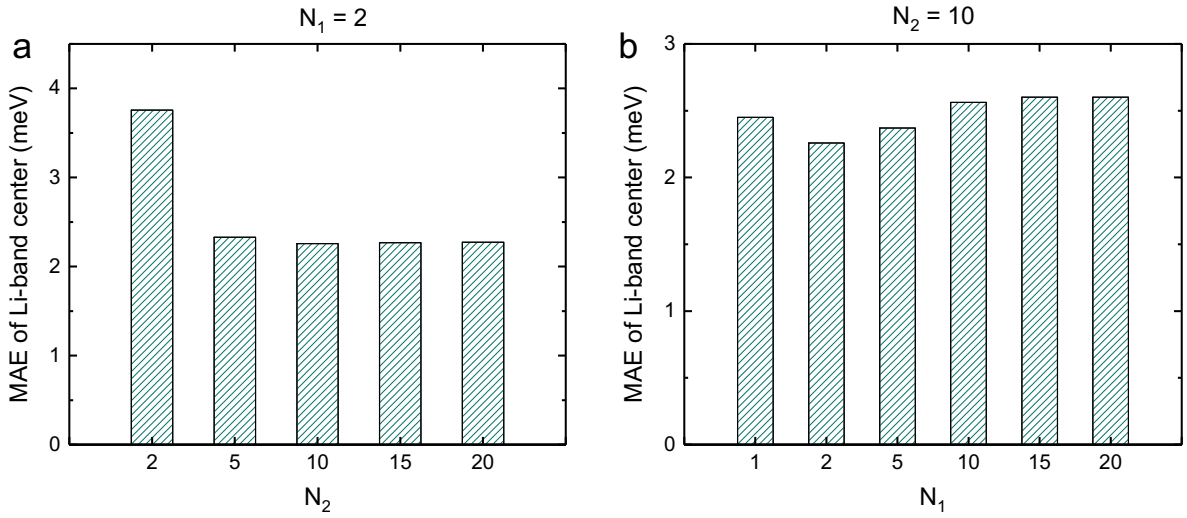

Figure S1. The mean absolute error of lithium-phonon band centers of the 53 compounds in Figure 2 as a function of the scaling parameter N_1 and N_2. Related to Figure 2.

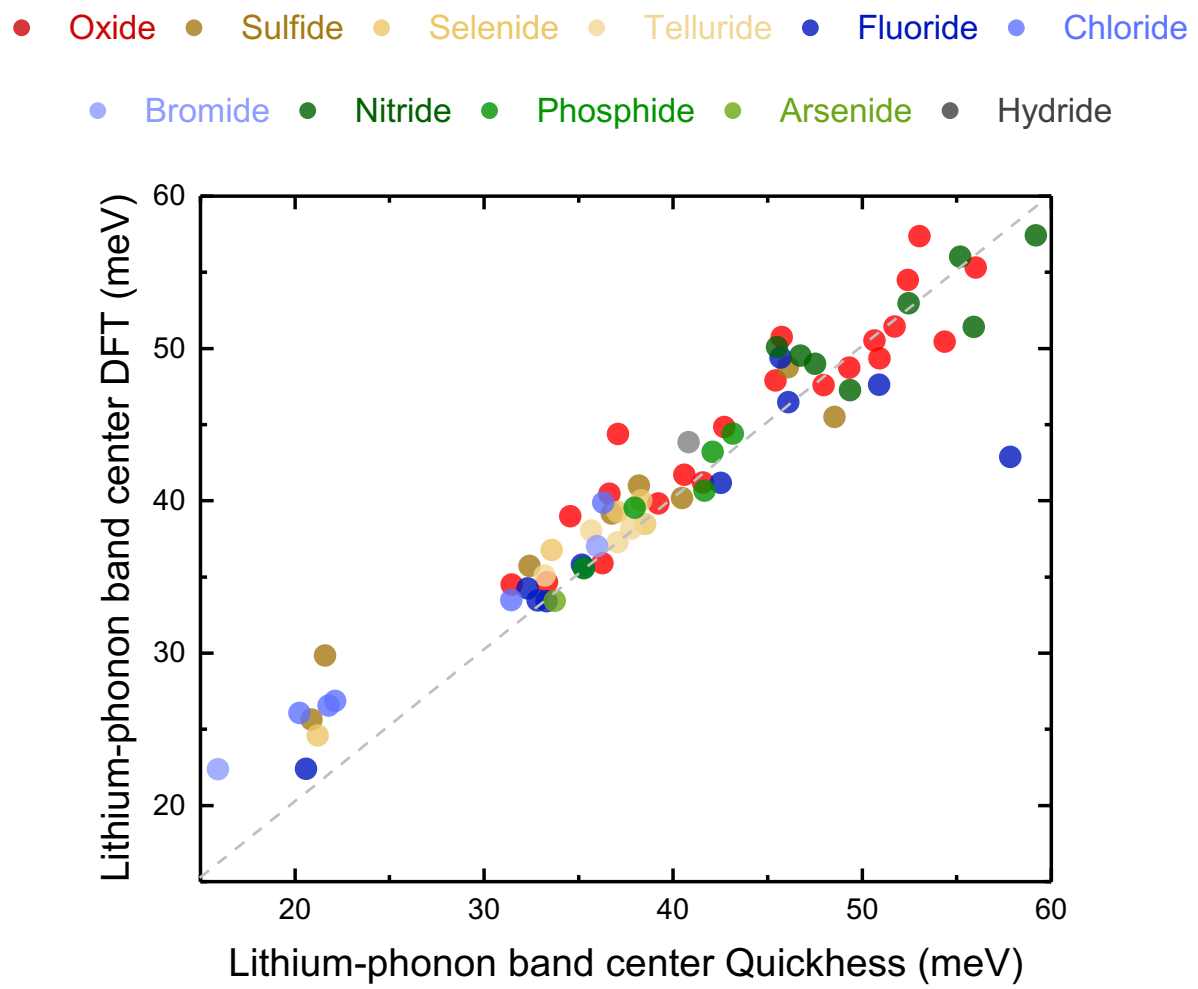

Figure S2. Comparison between the Li-phonon band centers of 71 compounds computed with *Quickhess* and full DFT calculations available in the Materials Project database. Related to Figure 2

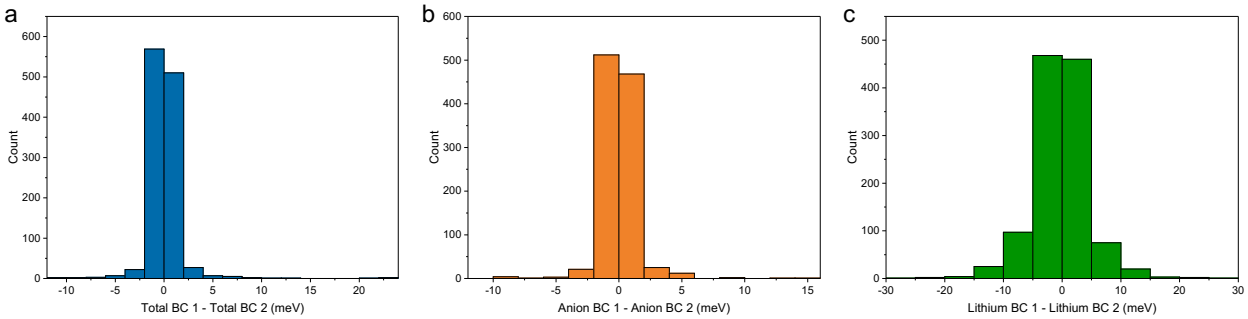

Figure S3. The difference between phonon band centers computed with two different sets of scaling parameters ($N_1 = 2$; $N_2 = 10$ and $N_1 = 5$; $N_2 = 10$) for all of the ~1200 compounds retained after pre-screening. Related to Figure 2 and 3.

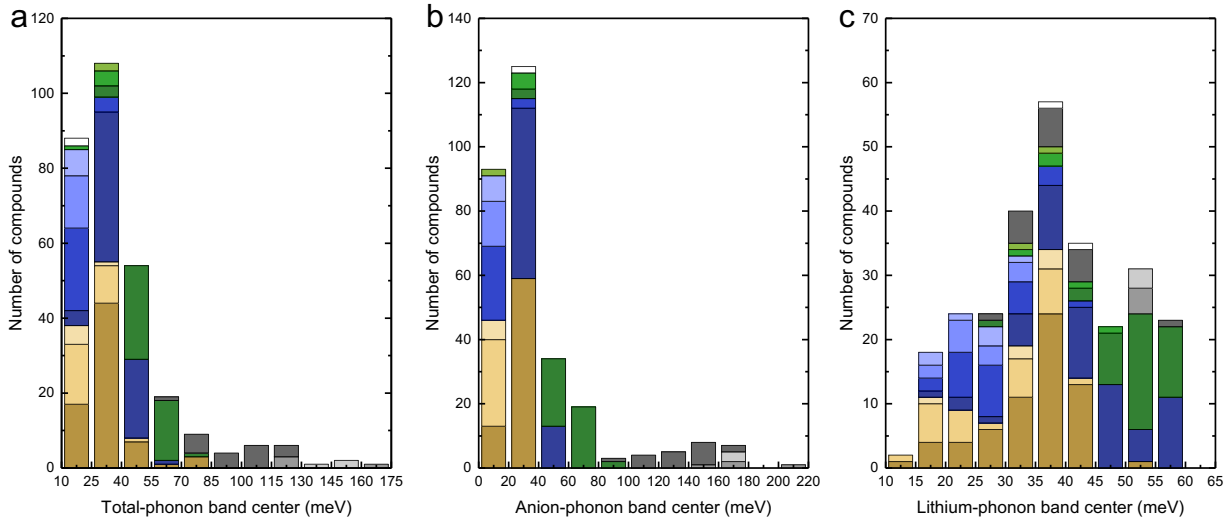

Figure S4. Histograms of a) Total-, b) Anion- and c) Lithium-phonon band centers for all chemistries excluding oxides. Related to Figure 3.

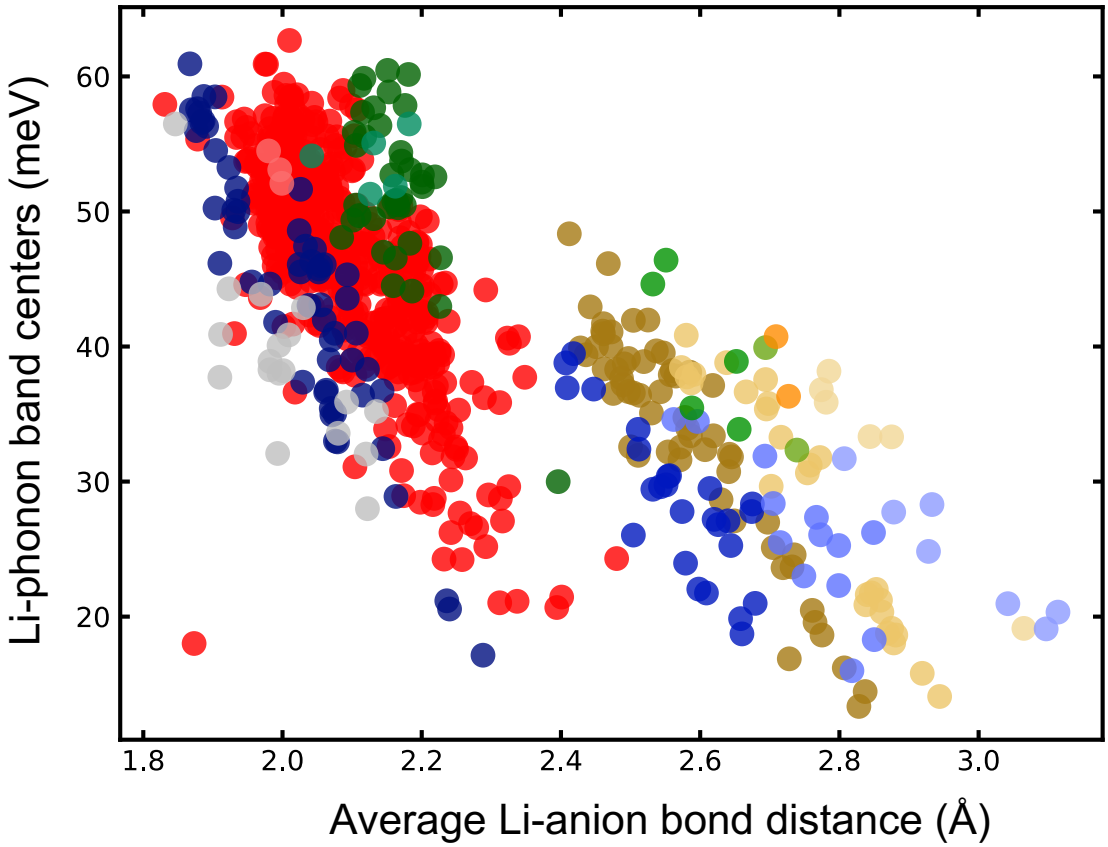

Figure S5. Correlation between the Li-phonon band centers and the average Li-anion bond length. Related to Figure 4.

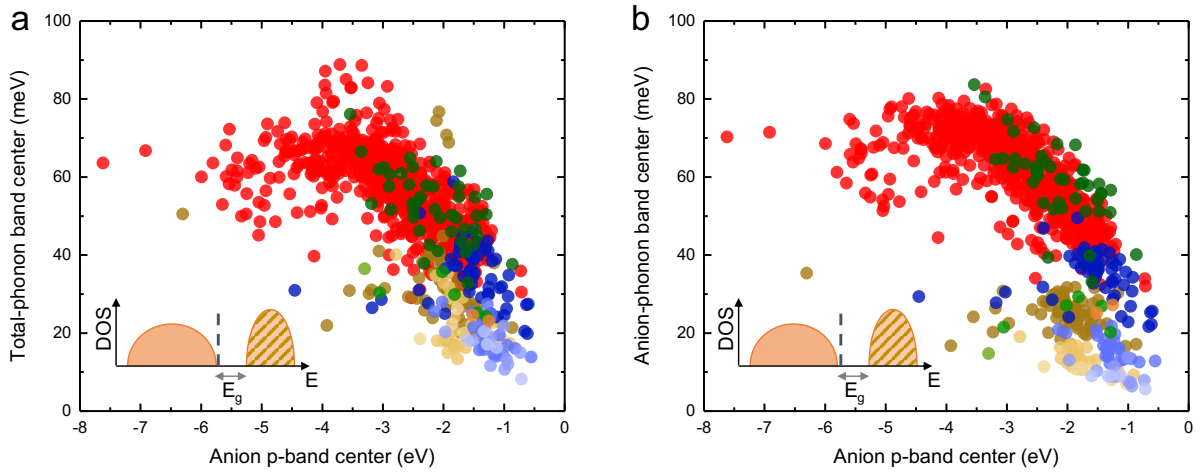

Figure S6. Correlation between a) Total- and b) Anion-phonon band center with the anion p-band centers. Hydrogen-containing compounds (hydrides, hydroxides and amides) were excluded due to the particular low mass of hydrogen and the difference in the nature of bonding which involves the s-orbital instead of p-orbitals. The inset shows the schematic of the anion-projected electronic DOS. The p-band centers were computed by integrating over the occupied states with respect to the top of the valence band indicated by the dashed line. Related to Figure 5.

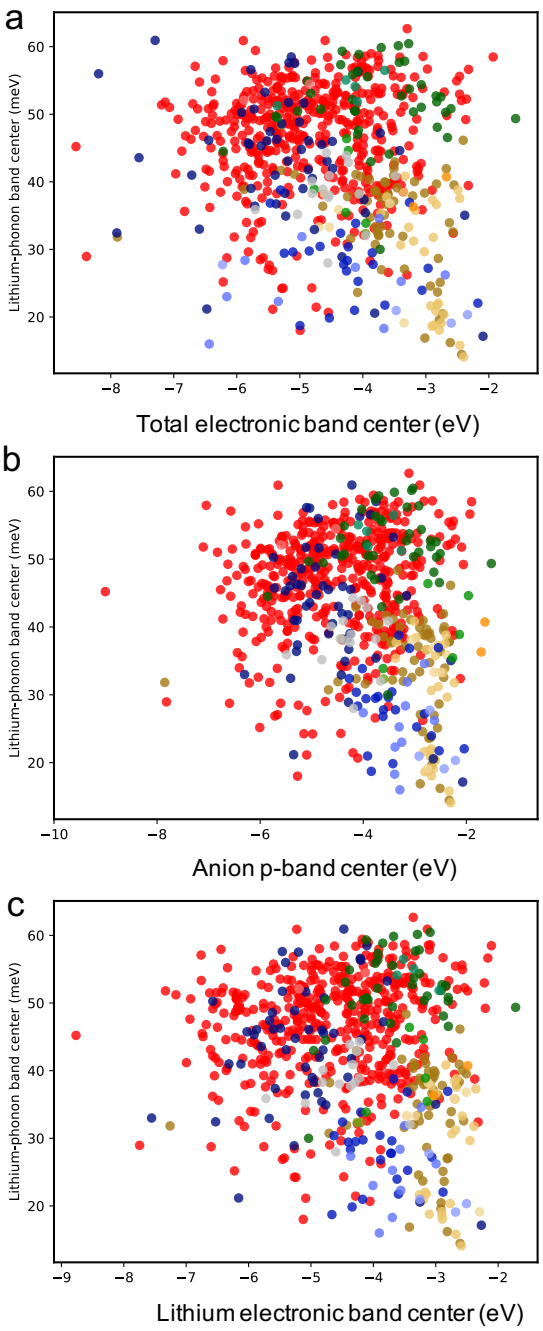

Figure S7. Absence of correlation between Li-phonon band center and a) Total electronic band centers b) anion p-band center and c) Lithium electronic band center. Related to Figure 5 and 6.

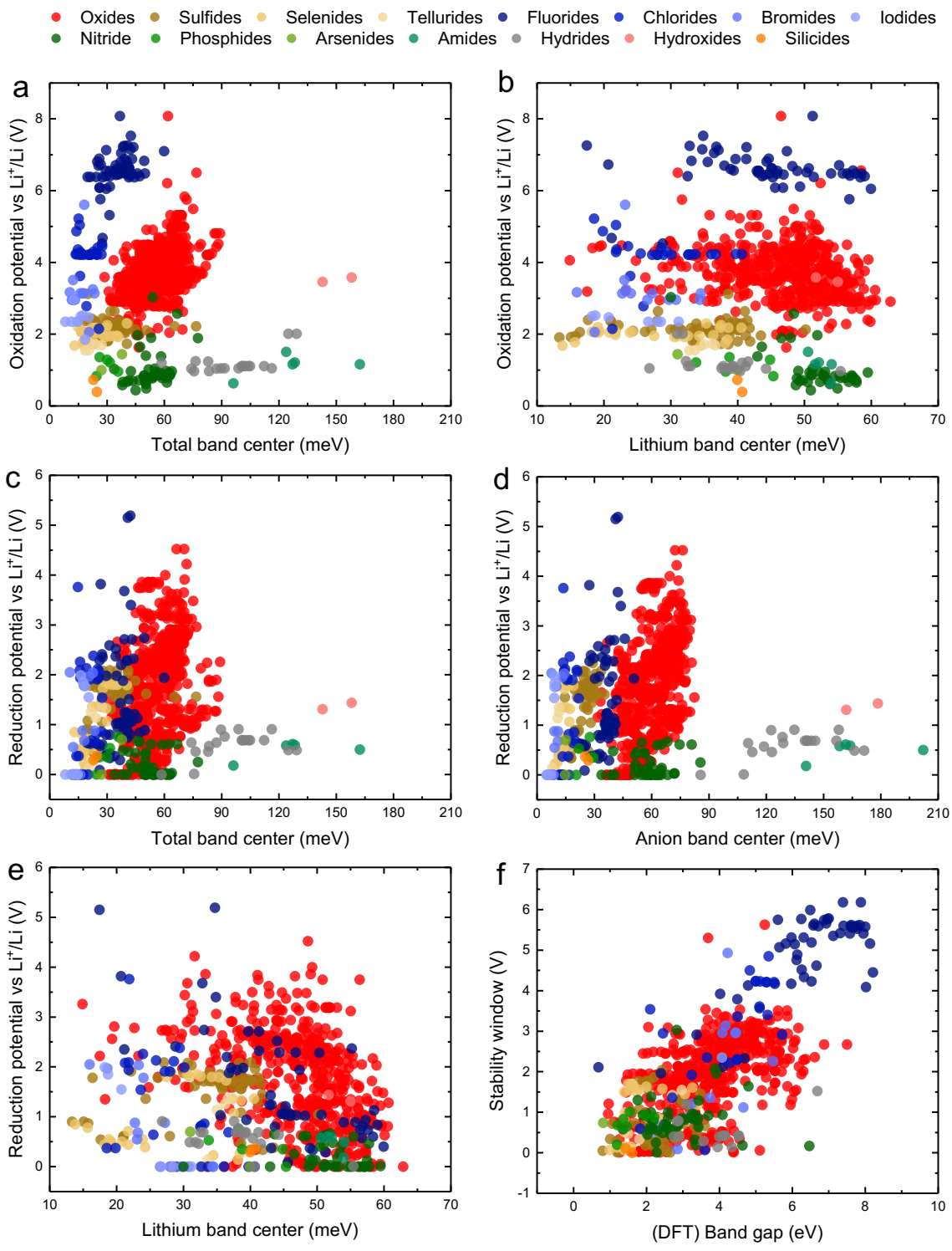

Figure S8. Correlation between oxidation potential and a). Total-phonon band centers b). Lithium-phonon band centers. Correlation between reduction potential and c). Total-phonon band centers d). Anion-phonon band centers e). Lithium-phonon band centers. f). Correlation between stability window and band gaps. Related to Figure 6.

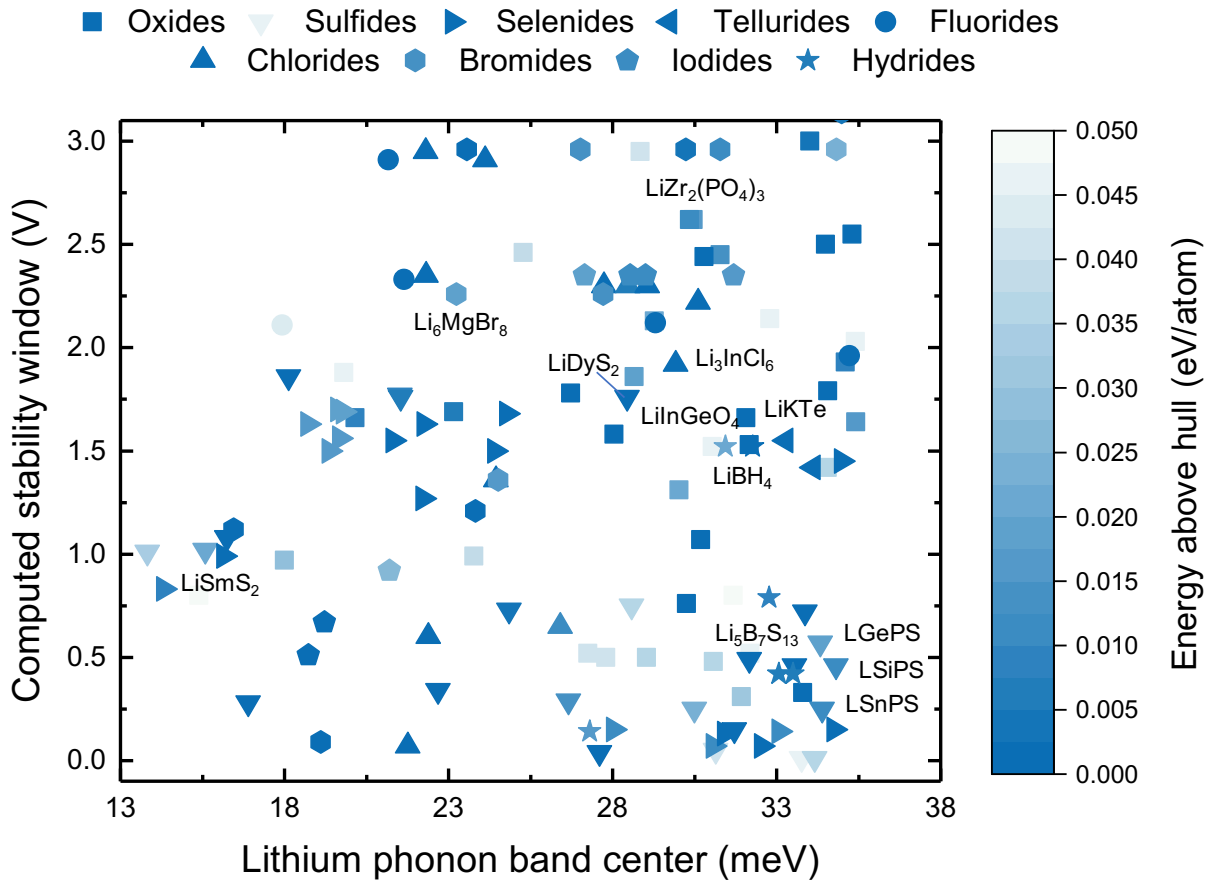

Figure S9. All compounds having stability window smaller than 3V and Li-phonon band center smaller than 35 meV along with their energy above hull. Compounds having non-zero energy above hull are thermodynamically unstable at 0K although they can be stabilized at higher temperature by entropic contributions. LGePS, LSiPS and LSnPS stand respectively for $Li_{10}GeP_2S_{12}$, $Li_{10}SiP_2S_{12}$ and $Li_{10}SnP_2S_{12}$. Related to Figure 7.

Table S1. Compounds with Li-phonon band centers smaller than 35 meV along with their stability window, energy above hull and the material id as appeared in the Materials Project database. Related to Figure 7.

Name	MP id	E_hull (eV/atom)	Li-band centers (meV)	Stability Window (V)
Li2PbO3	mp-22450	0	29.76	0.76
LiNbO3	mp-755559	0.0466	32.297	2.14
LiTa3O8	mp-559908	0.0139	30.778	2.45
LiGdO2	mp-754204	0.0402	28.342	2.95
LiErO2	mp-10971	0.0026	33.518	3
LiTa3O8	mp-7638	0	30.288	2.44
LiNO3	mp-8180	0	34.795	2.55
LiIO3	mp-22955	0.0091	34.595	1.93
LiNb3O8	mp-3368	0	31.571	1.66
LiNbO3	mp-1078377	0.0203	28.772	2.13
LiTa3O8	mp-757158	0.0384	24.783	2.46
LiNb(TeO4)3	mp-758389	0.0015	33.295	0.33
LiGe2(PO4)3	mp-541272	0.0015	27.54	1.58
LiP3W2O13	mp-763452	0.0477	31.178	0.8
Ba4Li(SbO4)3	mp-7971	0	26.219	1.78
LiIn(IO3)4	mp-973966	0	30.187	1.07
LiSn(PO3)3	mp-684503	0.0361	28.535	0.5
LiBiP2O7	mp-684109	0.0451	19.314	1.88
LiSb2P5O16	mp-684104	0.0471	30.541	1.52
LiZr2(PO4)3	mp-681439	0.0159	29.963	2.62
Li2P5WO15	mp-763414	0.0302	31.429	0.31
Li2Sn(PO3)4	mp-26855	0.0416	26.749	0.52
LiSn(PO3)3	mp-26897	0.0406	27.292	0.5
LiInGeO4	mp-17854	0	34.065	1.79
LiP2WO8	mp-763370	0.0488	14.895	0.8
LiSn(PO3)3	mp-758086	0.0464	31.686	0.52
LiZr2(PO4)3	mp-773068	0.0111	29.848	2.62
LiBiP2O7	mp-672979	0.0196	28.165	1.86
LiSn2(PO4)3	mp-562473	0.0053	22.662	1.69
Li2Pr(NO3)5	mp-555979	0	31.056	3.54
LiSbWO6	mp-19694	0.0368	34.053	1.42
LiGa(WO4)2	mp-19695	0.0218	29.531	1.31
LiSi6Bi9O26	mp-757434	0.0381	23.271	0.99
LiB(S2O7)2	mp-1020060	0	31.674	1.53
LiSi6Bi9O26	mp-772721	0.0282	17.502	0.97
Li2TlPCO7	mp-754034	0.0371	30.574	0.48
LiNbSn3(PO4)6	mp-767091	0.0091	19.654	1.66
K2LiTa6(PO8)3	mp-684817	0	33.994	2.5
LiMgAl3(SO4)6	mp-677680	0.017	34.913	1.64
Li3MgPCO7	mp-768190	0.0455	34.902	2.03
LiCa9Mg(PO4)7	mp-686484	0	18.274	3.05
LiCuS	mp-753371	0.0456	33.26	0.01
LiCuS	mp-766467	0.0361	33.657	0.01
LiSmS2	mp-34477	0	15.743	1.08
LiNdS2	mp-36791	0.0204	15.087	1.02

Li2B2S5	mp-29410	0	31.212	0.15
LiPrS2	mp-675419	0.0342	13.322	1.01
Li8Nb2S9	mp-769036	0.0424	30.648	0.05
LiAsS2	mp-555874	0	22.177	0.34
Li5B7S13	mp-532413	0	31.674	0.49
Li3NbS4	mp-769032	0	27.097	0.04
LiHoS2	mp-15790	0	17.622	1.86
LiSbS2	mp-14591	0.0138	26.161	0.29
LiDyS2	mp-15789	0	27.948	1.76
LiYS2	mp-33363	0.0084	21.02	1.77
LiDyS2	mp-33667	0.0069	21.045	1.76
LiSbS2	mp-1079885	0	16.4	0.28
Li7Y7ZrS16	mp-754856	0.0047	24.346	0.73
Li2Ga2GeS6	mp-554782	0.0361	28.086	0.75
Li7Y7Zr9S32	mp-767467	0.0004	33.364	0.72
Li10Sn(PS6)2	mp-721236	0.011	33.891	0.25
Li10Si(PS6)2	mp-720509	0	33.052	0.46
Li10Ge(PS6)2	mp-696138	0.0188	33.833	0.57
Li10Si(PS6)2	mp-696129	0.0112	34.31	0.46
Li10Sn(PS6)2	mp-696123	0.0227	29.995	0.25
RbLiSe	mp-9250	0	34.467	1.45
LiErSe2	mp-35205	0.0176	19.285	1.69
LiSmSe2	mp-35388	0	15.647	0.99
LiDySe2	mp-35717	0.0159	19.175	1.56
LiNdSe2	mp-37605	0.0076	13.81	0.83
LiYSe2	mp-37879	0.0176	19.112	1.7
LiTbSe2	mp-38695	0.0154	18.851	1.5
LiTbSe2	mp-15793	0	23.899	1.5
LiGdSe2	mp-15792	0	21.719	1.27
LiDySe2	mp-15795	0	20.807	1.55
LiHoSe2	mp-15796	0	21.747	1.63
LiErSe2	mp-15797	0	24.262	1.68
LiHoSe2	mp-33322	0.0168	18.208	1.63
Li10Sn(PSe6)2	mp-705516	0.0122	30.561	0.07
Li10Si(PSe6)2	mp-706277	0.0111	27.521	0.15
Li10Si(PSe6)2	mp-721253	0	34.245	0.15
Li10Sn(PSe6)2	mp-721252	0	32.03	0.07
Li10Ge(PSe6)2	mp-721239	0	30.904	0.13
Li10Ge(PSe6)2	mp-696127	0.0114	32.57	0.14
NaLiTe	mp-8754	0	33.621	1.42
KLiTe	mp-4495	0	32.79	1.55
LiAsF6	mp-9144	0	32.837	3.57
LiPF6	mp-9143	0	33.088	4.09
LiCuF4	mp-753541	0.0441	17.426	2.11
LiBiF6	mp-27419	0	34.716	1.96
LiSbF6	mp-3980	0	34.861	4.13
Cs2LiTlF6	mp-989562	0	20.661	2.91
LiTl2InF6	mp-989551	0	28.812	2.12
LiTl2GaF6	mp-989577	0	21.141	2.33
K2LiAlF6	mp-9839	0.0015	32.535	5.6

LiSnCl3	mp-998230	0.0109	25.901	0.65
Li3ErCl6	mp-676361	0	25.508	3.61
CsLiCl2	mp-23364	0	33.689	4.23
Li2ZnCl4	mp-23416	0.001	27.234	2.3
LiYb2Cl5	mp-23421	0.0189	28.914	4.21
Li2CdCl4	mp-38008	0	30.108	2.22
Li2MgCl4	mp-38684	0	32.655	3.4
LiGaCl3	mp-29344	0	21.256	0.07
CsLi3Cl4	mp-571666	0.0124	28.001	4.21
Li3InCl6	mp-676109	0	29.424	1.92
CsLi2Cl3	mp-569117	0.0042	32.635	4.21
Li10Mg7Cl24	mp-530738	0.0027	33.118	3.36
Li2ZnCl4	mp-22961	0.0053	27.967	2.3
LiGaCl4	mp-28341	0	28.563	2.3
LiAlCl4	mp-22983	0	23.62	2.91
Rb2LiInCl6	mp-989583	0	21.803	2.95
Rb2LiTlCl6	mp-989579	0	21.888	0.6
LiTl2InCl6	mp-989512	0	23.941	1.36
Cs2LiInCl6	mp-571527	0	21.815	2.35
Cs2LiYCl6	mp-567652	0	19.831	4.5
Cs2LiLuCl6	mp-570379	0	18.524	4.85
CsLi2Br3	mp-606680	0.0137	26.519	2.96
Li2ZnBr4	mp-28829	0.0172	24.016	1.36
Li6MgBr8	mp-29008	0.0199	22.737	2.26
Li3ErBr6	mp-37873	0	23.178	4.93
Cs2Li3Br5	mp-571409	0.0108	30.78	2.96
RbLiBr2	mp-28237	0.0048	34.486	3.14
LiGaBr4	mp-28326	0	23.315	1.21
LiGaBr3	mp-28327	0	18.607	0.09
CsLiBr2	mp-23057	0.0046	29.73	2.96
Cs2LiBr3	mp-1095674	0.0231	34.317	2.96
Li2MgBr4	mp-29009	0.0145	27.22	2.26
Cs2LiInBr6	mp-989405	0	15.956	1.12
Rb2LiDyBr6	mp-567628	0	23.059	2.96
Cs2Li3I5	mp-608311	0.0113	28.504	2.35
Li2ZnI4	mp-23497	0.0263	20.704	0.92
LiGaI4	mp-567967	0	18.723	0.67
LiInI4	mp-541001	0	18.231	0.51
Cs2Li3I5	mp-1080534	0.0115	28.035	2.35
Cs3LiI4	mp-569238	0.0183	26.648	2.35
CsLi2I3	mp-569055	0.0174	31.189	2.35
Sr4Li(BN2)3	mp-9723	0	29.999	3.03
LiBeP	mp-9915	0	33.782	0.68
LiBeAs	mp-9562	0	31.011	0.74
LiBeH3	mp-977148	0.0051	32.572	0.42
LiAlH4	mp-976291	0.0167	26.807	0.14
LiBH4	mp-30209	0	31.774	1.52
LiBeH3	mp-1079676	0.006	32.998	0.42
LiBH4	mp-1095543	0.0206	30.941	1.52
K2LiAlH6	mp-24411	0.0091	32.272	0.79

Transparent methods

Database and screening criteria

The structure of all compounds in our study were sourced from the Materials Project database(Jain et al., 2013) containing ~ 14,000 Li-containing compounds using the API functionality(Ong et al., 2015) implemented in the *Pymatgen* software package.(Ong et al., 2013) Four criteria were used to pre-screen all these compounds before proceeding to the computation of phonon band centers: (1) The stability of each compound was assessed based on their energy above hull, E_{hull} which is the distance between the point representing the compound in the phase diagram and the convex hull.(Ong et al., 2010; Ping Ong et al., 2008) Materials having $E_{hull} > 0$ are thermodynamically unstable at 0 K. However, if E_{hull} is not too large, the material can still be stable at finite temperatures due to the entropic contribution to the free energy. We set the threshold of E_{hull} to 50 meV/atom based on the observation that e.g. LGPS (space group $P4_2mc$) has $E_{hull} = 30$ meV/atom but can still be synthesized and is stable RT.(Kamaya et al., 2011) (2) The next criterion was to have a computed band gap of at least 1 eV in order to filter out compounds with too high electronic conductivity to be used as electrolytes. (3) We included only ternary, quaternary and quintenary compounds and excluded the binary compounds due to their rather restricted chemical space. (4) Finally, we excluded all compounds containing 3d transition elements, platinum-group elements and elements in the actinide series, due to concerns about cost, toxicity and internal redox-activity. After this pre-screening, ~ 1200 compounds were retained, and their phonon band center computed.

Detailed methodology of *Quickhess* method

The main idea of this method is that the eigenvalues of the Hessian matrix can be estimated with a single DFT force projection if reasonably good approximations to the eigenvectors are available. In the original implementation (Voss and Vegge, 2008) approximate eigenvectors were constructed from a point charge force field evaluated with Ewald summation and thus with negligible effort compared to a DFT calculation, and point charges were optimized to reproduce the DFT ground-state ionic positions. Here, instead of using Ewald summation, we screen the Coulomb interaction: $V_{screen} \sim exp(-Kr)/r$ with K=1/2Å^{-1} and sum in real space only. Charges are

not fitted but we simply use Bader charges. Neither of the two simplifications changes the trends in approximated phonon band centers. Following Voss *et al.* (Voss and Vegge, 2008), the Hessian matrix of this purely electrostatic force field is diagonalized to obtain the eigenvalues and eigenvectors (displacements) $\underline{u_i}$. From these eigenvectors, a special displacement $\underline{w}$ is constructed simply as a sum of all $\underline{u_i}$. The more accurate Hessian $\boldsymbol{H}$ eigenvalues h_i can be obtained by projecting the Hessian of a more accurate DFT Hamiltonian onto this displacement:

$$h_i \approx \underline{u_i}^{\mathrm{T}} \boldsymbol{H} \underline{w} \tag{S1}$$

The projection of the Hessian $\boldsymbol{H}$ onto $\underline{w}$ is approximated as the difference between the force on a new displaced configuration of the initial structure which is generated by applying the displacement $\underline{w}$ to the structure and the force on the initial structure:

$$\boldsymbol{H}\underline{w} \approx \frac{1}{\varepsilon}\left[\underline{\nabla}E\left(\underline{r_o} + \varepsilon\underline{w}\right) - \underline{\nabla}E\left(\underline{r_o}\right)\right] \tag{S2}$$

Where E is the (DFT) energy and $\underline{r_o}$ are the ground state coordinates and ε is a parameter to scale the displacement for the finite difference as defined in equation (2). If the initial configuration is a well relaxed structure, then the term $\underline{\nabla}E\left(\underline{r_o}\right)$ can be neglected. The parameter ε must be chosen carefully such that the induced force is well above numerical noise in the DFT calculations but also not too large potentially invalidating the harmonic approximation.

Synthesis and characterization of Li_3ErCl_6

The preparations and sample treatment for all compounds were carried out under argon atmosphere. Erbium chloride ($ErCl_3$, anhydrous, 99.9 %, Alfa Aesar) and lithium chloride (LiCl, ultra-dry, 99.9 %, Alfa Aesar) were mixed in the appropriate stoichiometric molar ratios, while adding approximately 2 wt% excess $ErCl_3$ relative to the total weighted mass to counter the loss of $ErCl_3$ during the hand grinding procedure. The mixture was then hand ground in an agate mortar to homogenize the powders and afterwards loaded into ball mill vials with a 30:1 mass ratio of the ZrO_2 milling media (3 mm in diameter) to the starting powder. The precursors were milled for 297 total cycles, while one cycle consists of 5 minutes of milling, followed by 15 minutes of rest time. Additionally, after every 99th cycle, the cups were opened and the powder homogenized manually

again to reduce the loss of sample on the inner walls of the vials. Crystallization of the as-prepared amorphous compounds were achieved by subsequent annealing for 1 h at 550 °C.

X-ray powder diffraction was carried out using an Empyrean powder diffractometer (PANalytical, Netherlands) with CuKa radiation (λ_1 = 1.54051 Å, λ_2 = 1.54051 Å) in Bragg–Brentano θ–θ geometry, and a PIXcel3D area detector with 255 measuring channels. Powder samples were placed on (911)-oriented silicon zero background holders that were sealed with Kapton foil under an argon atmosphere. Patterns were collected in the range of 10–90° 2θ with a step size of 0.026 and an exposure time of 150 s per step for the ball milled sample and 425 s for the subsequently annealed sample, to achieve a sufficiently high intensity and therefore acquire reliable lattice parameter values. Pawley fits(Pawley, 1981) were performed using the TOPAS-Academic V6 software package (Coelho, 2018). A manual background using 62 points was used, whereas the peak profiles were described by a Thompson–Cox–Hastings pseudo-Voigt function.

The ionic conductivities were measured by AC impedance spectroscopy, using pellets (1.4 mm average thickness, >80 % density for the amorphous compound (>75 % for the crystalline compound)) with vapor deposited gold layers (200 nm on each side; surface area of 0.53 cm^2). Electrochemical impedance analysis (EIS) was conducted in the temperature range of -40 °C to 60 °C using a VMP300 impedance analyzer (Biologic) at frequencies from 7 MHz to 100 mHz with an amplitude of 10 mV. All measurements were performed in pouch cells under an argon atmosphere.

Supplemental references

Coelho, A.A., 2018. *TOPAS* and *TOPAS-Academic* : an optimization program integrating computer algebra and crystallographic objects written in C++. Journal of Applied Crystallography 51, 210–218. https://doi.org/10.1107/S1600576718000183

Jain, A., Ong, S.P., Hautier, G., Chen, W., Richards, W.D., Dacek, S., Cholia, S., Gunter, D., Skinner, D., Ceder, G., Persson, K.A., 2013. Commentary: The Materials Project: A materials genome approach to accelerating materials innovation. APL Materials 1, 011002. https://doi.org/10.1063/1.4812323

Kamaya, N., Homma, K., Yamakawa, Y., Hirayama, M., Kanno, R., Yonemura, M., Kamiyama, T., Kato, Y., Hama, S., Kawamoto, K., Mitsui, A., 2011. A lithium superionic conductor. Nat Mater 10, 682–686. https://doi.org/10.1038/nmat3066

Ong, S.P., Cholia, S., Jain, A., Brafman, M., Gunter, D., Ceder, G., Persson, K.A., 2015. The Materials Application Programming Interface (API): A simple, flexible and efficient API for materials data based on REpresentational State Transfer (REST) principles. Computational Materials Science 97, 209–215. https://doi.org/10.1016/j.commatsci.2014.10.037

Ong, S.P., Jain, A., Hautier, G., Kang, B., Ceder, G., 2010. Thermal stabilities of delithiated olivine MPO4 (M=Fe, Mn) cathodes investigated using first principles calculations. Electrochemistry Communications 12, 427–430. https://doi.org/10.1016/j.elecom.2010.01.010

Ong, S.P., Richards, W.D., Jain, A., Hautier, G., Kocher, M., Cholia, S., Gunter, D., Chevrier, V.L., Persson, K.A., Ceder, G., 2013. Python Materials Genomics (pymatgen): A robust, open-source python library for materials analysis. Computational Materials Science 68, 314–319. https://doi.org/10.1016/j.commatsci.2012.10.028

Pawley, G.S., 1981. Unit-cell refinement from powder diffraction scans. Journal of Applied Crystallography 14, 357–361. https://doi.org/10.1107/S0021889881009618

Ping Ong, S., Wang, L., Kang, B., Ceder, G., 2008. Li−Fe−P−O2 Phase Diagram from First Principles Calculations. Chem. Mater. 20, 1798–1807. https://doi.org/10.1021/cm702327g

Voss, J., Vegge, T., 2008. Γ-point lattice free energy estimates from O(1) force calculations. The Journal of Chemical Physics 128, 184708. https://doi.org/10.1063/1.2919122